JGR Planets

Islands of ice on Mars and Pluto

Michael M. Sori[1] [ID], **Jonathan Bapst[1]** [ID], **Patricio Becerra[2]** [ID], and **Shane Byrne[1]** [ID]

[1]Lunar and Planetary Laboratory, University of Arizona, Tucson, AZ, USA, [2]Physikalisches Institut, Universität Bern, Bern, Switzerland

Abstract Ice sheets, such as the polar layered deposits (PLDs) of Mars, are of great interest as records of past climate. Smaller outlier ice deposits near the north and south PLDs are likely more sensitive to climate changes and thus may hold information about more recent climate history. However, the southern outlier deposits have largely remained unmapped and unanalyzed. Here, we identify 31 deposits near, but separated from, Mars's south PLDs, all of which are located within impact craters >15 km in diameter. On the basis of morphology, radar analysis, physical similarity to portions of the PLD margin, and overall similarity to previously described deposits in Mars's north polar region, we conclude that these deposits are primarily composed of water ice. An additional 66 craters contain smaller depositional features, some of which may be remnant ice deposits. The 31 outlier ice deposits represent a previously unquantified inventory of water on Mars, with a total volume between 15,000 and 38,000 km³. In addition, we identify five analogous outlier nitrogen ice deposits located within impact craters near Sputnik Planitia, the large nitrogen ice sheet on Pluto. Although important differences exist between Mars and Pluto, broad physical similarities between the two cases suggest that the topography and microclimates of impact craters cause them to be favorable locations for volatile accumulation and/or retention throughout the Solar System.

Plain Language Summary Mapping and quantifying ice on the surfaces of planets are of interest for a variety of reasons relating to science and exploration. Here, we identify 31 ice deposits located within craters in the south polar region of Mars, near the massive southern polar ice sheet. These new 31 ice deposits represent an inventory of more than 10 trillion cubic meters of solid water, similar to but greater in number and volume than previously studied features near the north pole. Similar features of nitrogen ice may exist in craters on Pluto, suggesting that craters are a favorable location for the accumulation or preservation of ices throughout the Solar System.

1. Introduction

Ice deposits on planetary surfaces are of great scientific interest because they serve as a record of geological processes involving the interaction of volatiles, topography, atmospheres, and climate. The most well-studied large, extraterrestrial ice sheet is the north polar layered deposit (NPLD) of Mars (see review in Byrne, 2009). Many studies have used remote sensing observations of the NPLD in an attempt to quantify Martian paleoclimate, with a particular focus on correlating icy stratigraphy with the planet's orbital variations. These studies have yielded promising but uncertain results (e.g., Becerra et al., 2017; Cutts & Lewis, 1982; Laskar et al., 2002; Milkovich & Head, 2005; Perron & Huybers, 2009; Sori et al., 2014). The ultimate goal of deciphering the paleoclimate record in polar ice on Mars is progressing but incomplete.

One way to move forward is to examine polar ice deposits that are separate from the larger polar layered deposits (PLDs). Outlying ice deposits peripheral to the main polar ice sheets may be more sensitive to climatic changes because of their lower latitudes. In the northern hemisphere of Mars, 18 ice deposits have been identified within impact craters at high latitudes (Conway et al., 2012); two examples are shown in Figure 1. The deposits are near, but separate from, the NPLD and have been noted by other authors (e.g., Krasilnikov et al., 2018). These outliers, which we hereafter term "ice mounds," have a dome-like, convex morphology and are located at >70° latitude on the floors of impact craters >10 km in diameter but are often off-center, with space between the margin of the ice mound and the bottom of the crater wall (e.g., Figure 1b). Thicknesses of the mounds vary, and some have exposed ice layering or dune cover. Radar analysis has quantified the ice content and volume of one particular ice mound in Korolev crater (Brothers & Holt, 2016), while image analysis and theoretical models have constrained the annual mass balance of the same mound, plus one in Louth crater (Bapst et al., 2018).
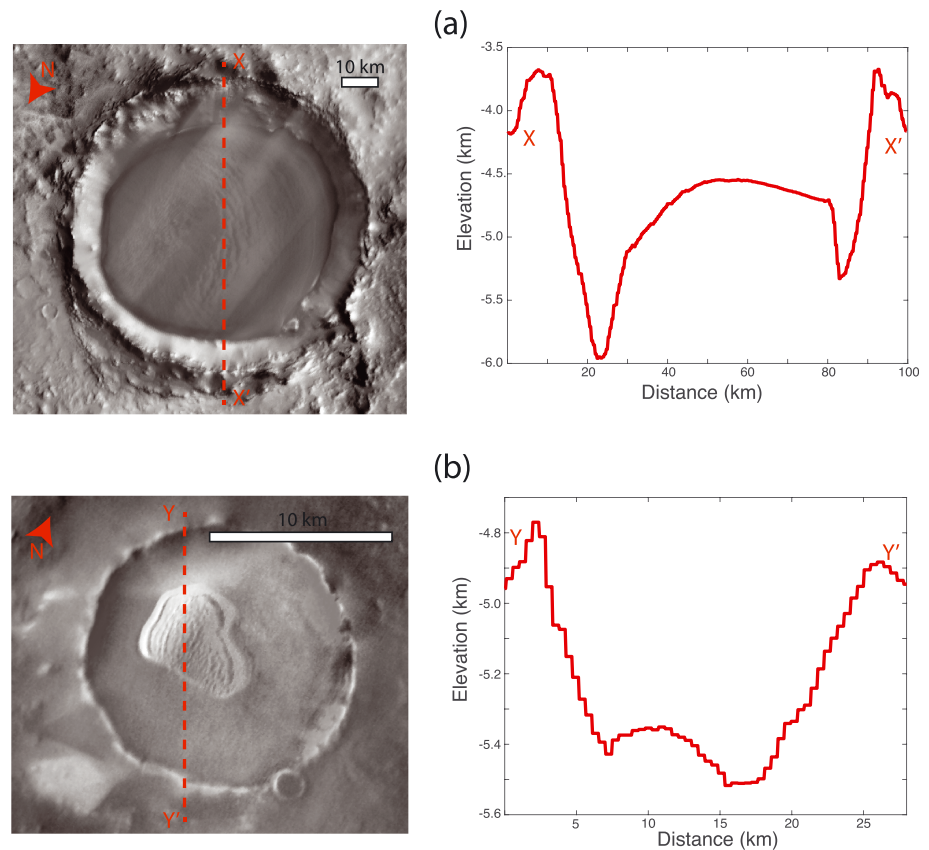
Figure 1. Examples of crater deposits identified as ice mounds in the north polar region of Mars by Conway et al. (2012). (a) Daytime Thermal Emission Imaging System infrared mosaic of Korolev crater at 72.8°N, 164.5°E with Mars Orbiter Laser Altimeter topographic profile. (b) The same data as for (a) but for an unnamed crater at 74.6°N, 346.9°E. All scale bars are 10 km in length.

Important questions about the origin and evolution of these northern ice mounds remain unanswered. Possible formation mechanisms include local atmospheric deposition of ice directly onto the crater floor or the retreat of a previously more extensive NPLD. An alternative mechanism not involving an atmospheric source of ice is the activation of a hydrothermal system in the crust, either directly following the impact that formed the crater (Rathbun & Squyres, 2002) or later (Russell & Head, 2002). Stratigraphic analysis of layering in the mounds suggests some role for local atmospheric accumulation, but it is unknown whether this process was initiated on a crater floor solely as a result of the microclimate of the crater or if remnants of ancient ice from a formerly more extensive NPLD are required (Conway et al., 2012). The age of the ice mounds, and therefore the paleoclimate record contained therein, is uncertain. One way to understand the origin and evolution of the ice mounds is to determine whether they exist elsewhere. Are ice mounds an inevitable consequence of ice sheet deposition on a cratered landscape, or is there something about the geology or climate of the north polar region of Mars that makes this area particularly favorable?

We address this question by searching for, cataloging, and analyzing potential ice mounds near the south polar layered deposit (SPLD) of Mars. Like the NPLD, the SPLD is a ~1,000-km-wide sheet of water ice that has been studied, in part, for its potential paleoclimate record (albeit less so than the NPLD). Geologic mapping (Skinner et al., 2006; Tanaka & Kolb, 2001) shows that crater deposits also exist in the region. However, no peer-reviewed publication to date has comprehensively cataloged them, although the features are the subject of a student's Master's thesis (Westbrook, 2009). Here, we catalog and analyze these features using a variety of data sets, including images, topography, and radar.

Additionally, we search for similar features near another large extraterrestrial ice sheet in the solar system: Sputnik Planitia of Pluto. Many important differences exist between Sputnik Planitia and the PLDs of Mars,

including ice composition (mostly nitrogen ice in Sputnik Planitia (Moore et al., 2016) and mostly water ice in the PLDs) and the atmospheric environment (~1 Pa of mostly nitrogen at Pluto (Gladstone et al., 2016) and ~600 Pa of mostly carbon dioxide at Mars). Nonetheless, Sputnik Planitia is also an ~1,000-km-wide, few kilomter-thick ice sheet in a cratered landscape that exists at the latitude that is thermally favorable for volatile deposition according to the planet's orbital parameters and links climate to other planetary processes (Keane et al., 2016; Nimmo et al., 2016). Therefore, it would be useful for understanding ice mound formation to know whether outlier ice deposits exist in craters near Sputnik Planitia. As is the case in the south polar region of Mars, geologic mapping suggests that icy outliers exist near Sputnik Planitia (White et al., 2017), but they have not yet been thoroughly investigated.

The scope of this paper is to identify deposits within craters near the SPLD and assess the likelihood that they are analogous to the ice mounds near the NPLD described by Conway et al. (2012). We do the same for craters near Sputnik Planitia on Pluto, although results are more speculative due to the lower number and lower resolution of available data sets there. For each candidate ice mound, we analyze the physical properties of the deposit and its host crater and discuss the implications of these results for the origin and evolution of ice deposits that are outliers to large ice sheets. In the future, our catalog of features will enhance sophisticated paleoclimate and atmospheric modeling, as well as thermophysical studies.

2. Methods

2.1. Identification and Measurement of Deposits

We used a combination of images and topographic data to search for and analyze potential icy outliers in the south polar region of Mars. We used the Java Mission-planning and Analysis for Remote Sensing software (Christensen et al., 2009) to search daytime mosaics of infrared (IR) images (Edwards et al., 2011) from the Thermal Emission Imaging System (THEMIS) aboard the Mars Odyssey orbiter, mosaics of images from the Mars Orbiter Camera (Malin & Edgett, 2001) aboard the Mars Global Surveyor, and shaded relief maps constructed from topographic data from the Mars Orbiter Laser Altimeter (MOLA; Smith et al., 2001) aboard the Mars Global Surveyor. We inspected the region poleward of 60°S latitude, searching for positive relief features located within impact craters. The THEMIS IR mosaic has a resolution of 100 m/pixel (Edwards et al., 2011), the Mars Orbiter Camera mosaic has a resolution of 230 m/pixel, and the MOLA topographic map has a lateral resolution <500 m/pixel globally, <150 m/pixel near the poles, and has a vertical precision of <1 m (Smith et al., 2001).

We identified craters with clear positive relief deposits on their floors. This identification excludes central peaks of complex craters, which are located at the center of the crater, do not have the convex-up slopes characteristic of ice mounds identified in the northern polar region (Conway et al., 2012), and are small in extent (<10% of the area of the crater floor). We do not consider bright albedo as a necessary identification criterion because of the possibility of a darker lag deposit overlying potential ice, which is observed for some of the cases in the north (Conway et al., 2012). We do not consider or record craters that lie entirely within the main SPLD unit, such as those identified by Landis et al. (2018).

We cataloged three types of deposits. The first type comprises deposits that are large relative to the crater size and have a dome-like, convex-up topography. They are roughly circular in plan view, with diameters that are approximately half of the crater diameter or greater. They are spatially separated from the contiguous SPLD as mapped by Skinner et al. (2006). We call these circumpolar crater filling deposits (CCFDs), and they are the main subject of this work. Note that the word "filling" refers to the large surface area of the crater floor that the deposits occupy and does not necessarily imply that the topographic relief of the mound is equal to the crater depth or that there is an equal volume between the crater cavity and the deposit. Examples of CCFDs are shown in Figures 2a and 2b, with a typical topographic profile of a CCFD shown in Figure 2f. All CCFDs are shown in the supporting information (Figure S1 in the supporting information).

The second type includes crater deposits with similar morphology and surface area as the CCFDs but are continuous on at least one side with the SPLD and thus can be considered part of the SPLD margin. These types are called marginal SPLD deposits and have been the subject of prior stress modeling studies (Banks & Pelletier, 2008). Marginal deposits are by definition not considered as outlier deposits but are cataloged and measured because they may elucidate the origin of CCFDs. An example is shown in Figure 2c. Note
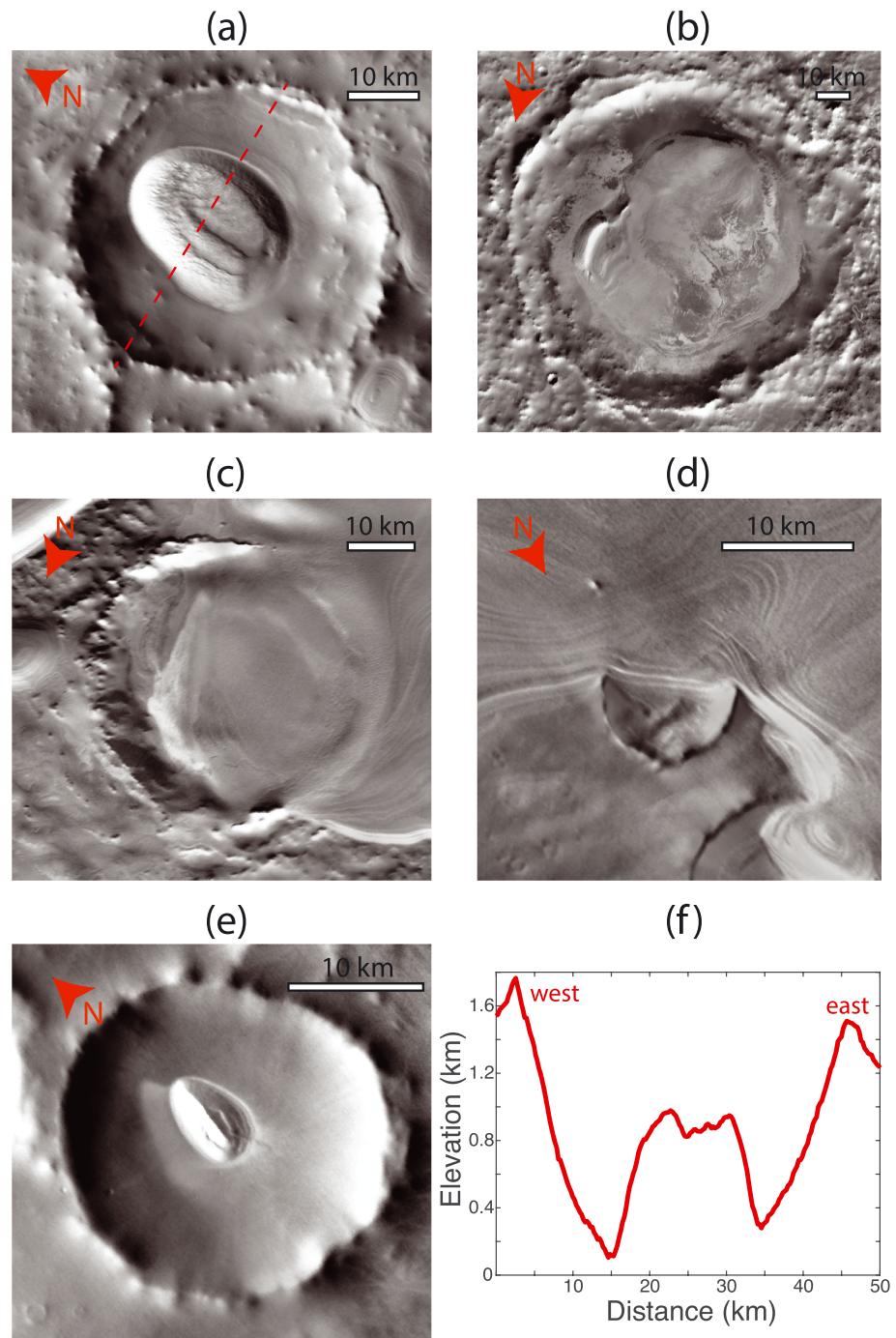
Figure 2. Examples of crater deposits from the daytime Thermal Emission Imaging System infrared mosaic in the south polar region of Mars. (a) Circumpolar crater filling deposit (CCFD) in an unnamed crater at 70.5°S, 159.0°E. (b) "Stacked" CCFD in South crater at 77.0°S, 22.1°E. (c) Marginal deposit in Elim crater at 80.1°S, 96.7°E. (d) The south polar layered deposit overprinting an unnamed crater at 80.6°S, 130.2°E; we do not consider this a CCFD, marginal, or irregular deposit. (e) Irregular deposit in unnamed crater at 70.0°S, 181.4°E. (f) West-east topographic profile from Mars Orbiter Laser Altimeter data through the CCFD in (a), with location represented by the dashed line in (a). All scale bars are 10 km in length.

that marginal deposits do not include every instance of the margin of the SPLD overlying an impact crater. In order to be cataloged as a marginal deposit, the deposit must have convex topography that occupies a substantial portion of the crater floor. This choice is made in an attempt to identify locations where the

presence of an impact crater was important in the origin or evolution of a deposit, as opposed to locations where the SPLD margin happens to coincide with a crater by chance. An example where the SPLD margin overlies a crater, but is not considered a marginal deposit, is shown in Figure 2d. A recently discovered impact crater at the northwestern edge of the Greenland ice sheet (Kjær et al., 2018) contains the Hiawatha glacier, potentially representing a terrestrial analogy to marginal deposits on Mars.

The third type involves crater deposits of positive relief that are clearly not central peaks but fail some of the criteria to be considered CCFDs. In most cases, the failed criterion is that they occupy a very small area (<10%, often <1%) of the crater floor. In other cases, they are crescent shaped instead of circular and have low topographic relief. We call this type irregular deposits. We consider the possibility that they are related to CCFDs, perhaps remnants of CCFDs (section 4.3). Our overall approach is to be inclusive in the identification of irregular deposits so that future researchers may use our inventory to make judgements according to their own goals but to be conservative in applying the CCFD designation to increase confidence that we are correctly identifying a common class of features in this paper. Figure 2e shows an example of an irregular deposit.

Measurements of the physical properties of the deposits were made using THEMIS images and MOLA gridded polar topography. Previous work has found that MOLA gridded topography is sufficient for analysis of craters with diameters greater than a few kilometers (Stewart & Valiant, 2006); all craters cataloged here are tens of kilometers in diameter (see section 3.1). We similarly find that MOLA gridded topography is appropriate (see supporting information). For each deposit, we extracted eight MOLA topographic profiles through the center of the deposit, which were along directions of N-S, NNE-SSW, NE-SW, ENE-WSW, E-W, ESE-WNW, SE-NW, and SSE-NNW. These profiles extended to the crater rim on either side. We noted which parts of the topographic profiles corresponded to the deposit by overlying the profile atop the THEMIS IR mosaic. We considered the average of the diameters of these parts of the eight profiles to be the diameter of the deposit. We considered the standard deviation of the eight profile diameters the uncertainty. Our reported uncertainties for diameters thus primarily represent how much the plan view shape of a deposit deviates from a circle, rather than instrument or measurement error. We measured the apparent topographic relief as the difference between the maximum elevation of the deposit and the elevation of the crater floor. The elevation of the crater floor is the average of the minima of the topographic profiles, excluding obvious smaller impact craters located on the crater floor. We did not include minima in profiles that correspond to a location where the deposit directly abuts the crater wall because we interpret that minimum to not necessarily represent the crater floor. We considered the standard deviation of the included minima as the uncertainty of the measurement. Our reported uncertainties for apparent topographic relief thus primarily represent our ability to identify the elevation of the crater floor. Additional physical properties that we measured to characterize the deposits included the shortest distance between each crater deposit and the main contiguous SPLD and the direction and magnitude of offset of deposits that are not centered on the crater center. The direction and magnitude of the offset are defined by the vector that connects the center of the crater to the center of the deposit.

Measurements of the physical properties of each deposit's host crater were made using MOLA topography and a previously published Mars crater database (Robbins & Hynek, 2012). For each crater that hosts a deposit, the rim-to-rim diameter was taken from the Robbins and Hynek (2012) database. Two methods of estimating crater rim-to-floor depths were considered. The first method was by taking the difference between the rim elevation (from the Robbins & Hynek, 2012 database) and floor elevation (from our measurements described in the previous paragraph), yielding an "apparent crater depth." This method is appropriate for the irregular deposits that typically cover a small area of the crater floor but likely yields an underestimate of crater depth for craters that host CCFDs and marginal deposits. In these cases, we additionally consider the "derived crater depth" d given by an empirically derived formula as a function of crater diameter D in the Martian polar regions (Garvin et al., 2000), where $d = 0.03D^{1.04}$. The thickness of a CCFD or marginal deposit is similarly calculated using these two methods. One method assumes that deposit thickness is the apparent topographic relief described in the previous paragraph, and the second method assumes that the thickness is the difference between the maximum elevation of the deposit and the floor elevation as predicted by the Garvin et al. (2000) relationship. The two methods yield lower and upper bounds on the deposit thickness, and we refer to them as the "apparent mound relief" and "derived mound relief," respectively. Volumes are similarly calculated with two methods. The volume of a CCFD is given by $\pi (D_{CCFD}/2)^2 h$, where D_{CCFD} is

our calculated deposit diameter. In the first method, h is the average elevation among topographic profiles for the CCFD; in the second method, h is the average elevation among topographic profiles plus the difference between derived mound relief and apparent mound relief. As with the mound thickness, these two methods yield lower and upper bounds on the deposit volume, respectively.

High-resolution images allow for detailed study of some deposits. Craters with available images from the High Resolution Imaging Science Experiment (HiRISE; resolution of ~25 cm/pixel; McEwen et al., 2007) aboard the Mars Reconnaissance Orbiter were searched for noteworthy geological details, including layer exposures and dune cover. These characteristics are observed on some northern ice mounds (Conway et al., 2012). A lack of detection of dunes or exposed layers by HiRISE images does not necessarily imply that these features are absent because the image footprint usually does not cover the entirety of the deposit.

A similar methodology was used to search for and analyze outlying ice deposits on Pluto. Compared to Mars, fewer data sets are available and they have lower resolution, but they are sufficient to identify kilometer-scale features in the encounter hemisphere. All Pluto data come from observations by the New Horizons spacecraft (Stern, Bagenal, et al., 2015). We searched all images from the Long-Range Reconnaissance Imager for evidence of bright albedo features in craters outlying Sputnik Planitia. For each anomalously bright feature, we analyzed topography from a global mosaic constructed from Long-Range Reconnaissance Imager and Multispectral Visible Imaging Camera observations (Schenk et al., 2018), recording the same attributes as we did for Mars. Derived crater depths for Pluto come scaling the measured diameters according to predicted depth/diameter scaling laws (Stern, Porter, et al., 2015). Resolution is variable across the surface of Pluto, and topographic data are not available everywhere on the planet, but it does exist in every location where we identified a potential crater ice deposit. We additionally searched for topographic mounds in each crater >20 km in diameter that is <500 km away from Sputnik Planitia to account for the possibility of crater deposits that do not have anomalously bright albedo at the surface.

2.2. Radar Analysis

For some deposits on Mars, we also analyzed radar data from the Shallow Radar (SHARAD) instrument aboard Mars Reconnaissance Orbiter (Seu et al., 2007). SHARAD collects returns of radar power as a function of delay time, also known as radargrams, along tracks over the Martian surface. Reflected power is concentrated primarily at the surface and also when the radar signal travels between two materials of different dielectric properties, such as ice and rock, because some power is reflected back at those material interfaces. The material property that controls how the radar signal propagates through a medium is the dielectric permittivity. The dielectric permittivity ε is a complex number, where the real component, ε', is related to energy storage and the imaginary component, ε'', is related to energy loss (e.g., Olhoeft, 2003). Here, we consider the real component, ε', as it is more direct to calculate from SHARAD observations when there exists a topographic constraint on the location of a material interface (e.g., Bramson et al., 2015). The imaginary component ε'' is more sensitive to mineralogical assumptions and less straightforward to estimate, although can be useful and may be worthy of future consideration (Campbell & Morgan, 2018). For the case of two-layered materials in the Martian subsurface, the real component of dielectric permittivity in the upper layer is given by $\varepsilon' = (ct/z)^2$, where c is the speed of light in vacuum, t is the one-way delay between the surface and the material interface, and z is the thickness of the upper layer.

We can use SHARAD radargrams to infer ε' of crater deposit material if certain conditions are met. If a radargram track passes through the center of a CCFD and contains a radar reflector beneath the surface reflector, we may consider the radargram further by assuming that the subsurface reflector represents the interface between the deposit and the underlying bedrock. Our estimates of deposit thickness provide an independent estimate for z, and the real component of the dielectric permittivity for the deposit material can be calculated from the equation above. This technique is similar to SHARAD-derived constraints on thicknesses of midlatitude ice sheets (Bramson et al., 2015) and opposite to previous SHARAD analysis of a crater deposit in the north polar region (Brothers & Holt, 2016), where dielectric permittivity was assumed in order to infer deposit depth because the composition of that deposit was already known.

In order to be confident in the validity of the assumption that a subsurface reflector represents the bottom of the CCFD, we must reject the alternative that this reflector is caused by "clutter" or internal layering within the deposit. Clutter occurs when the instrument detects reflections of the radar signal from off-nadir
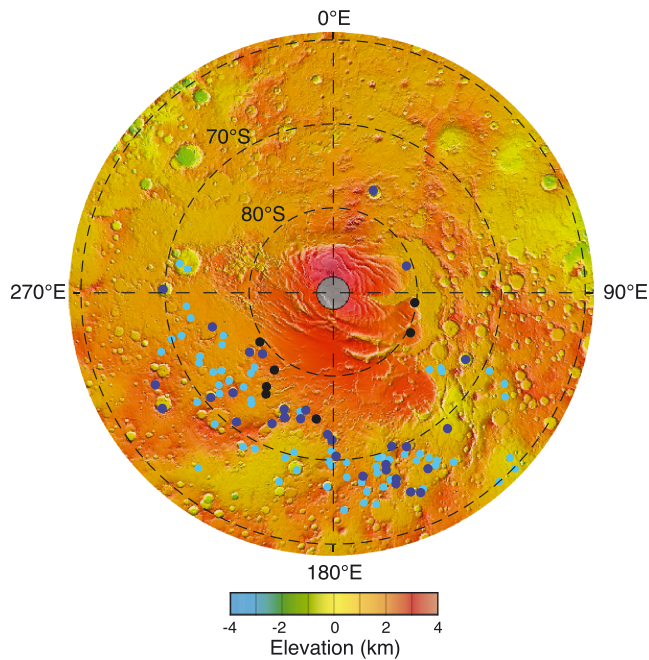
Figure 3. Locations of circumpolar crater filling deposits (dark blue points), marginal deposits (black points), and irregular deposits (light blue points) on a southern polar projection of elevation represented by Mars Orbiter Laser Altimeter-derived colored shaded relief.

topography that happen to arrive at similar delay times as those from real subsurface interfaces; this phenomenon can effectively mimic a subsurface material interface. In order to distinguish true subsurface reflectors in our selected radargrams, we compare them to clutter simulations generated using topographic data (Choudhary et al., 2016). Because it has been shown that MOLA-based clutter simulations do not always capture all important off-nadir reflections due to crater topography (Putzig et al., 2014), we consider clutter simulations generated using higher-resolution topography derived from High Resolution Stereo Camera (HRSC) images. HRSC digital elevation models (DEMs) are only available in a few locations in the south polar region but are necessary to have confidence in the results. The simulations use HRSC DEMs to generate artificial radargrams based solely on the surface reflection. These artificial radargrams are commonly used to discriminate clutter from subsurface reflections in both terrestrial studies (Holt et al., 2006) and Martian remote radar analyses (e.g., Brothers & Holt, 2016; Picardi et al., 2005). We therefore only infer ε' for radargrams with subsurface reflectors that do not also appear in the clutter simulations. We note that radar-based results are nonunique, and any inferences drawn from radar analysis about CCFD composition must be consistent with other observations, such as geomorphology, in order to yield confident interpretation.

When a value of ε' is inferred, it is compared to values of ε' of relevant Martian materials. For pure water ice, we assume that the value of ε' is 3.15 (Brouet et al., 2016; Matsuoka et al., 1997). The value of ε' for solid basalt is dependent on material properties such as vesicularity, bulk density, and mineralogy (e.g., Campbell & Ulrichs, 1969; Pettinelli et al., 2005) but is consistently greater than that of water ice; we assume a nominal value of 7.54 (Rust et al., 1999). We also consider combinations of rock, ice, and air (we assume the value of ε' of air to be 1); for these cases, we compare the inferred value of ε' from SHARAD observations to the value of ε' of the mixed material computed in two different ways. In the first way, we assume that the value for the mixed material raised to the power of 1/2.7 is given by the volumetrically weighted sum of each individual component raised to the power of 1/2.7 (Bramson et al., 2015; Nerozzi & Holt, 2019; Stillman et al., 2010):

$$\varepsilon'^{0.37} = 3.15^{0.37}V_i + 7.54^{0.37}V_r + 1^{0.37}V_a. \tag{1}$$

V_i, V_r, and V_a are the volumetric fractions of ice, rock (assumed to be basalt), and air (or porosity), respectively. In the second way, we derive the value for the mixed material by an empirically derived mixing model (Brouet et al., 2019):

$$\varepsilon' = \left(16.94^{\frac{\rho_r V_r}{\rho_r V_r + \rho_i V_i}} + 2.00\right)^{1-V_a} + \frac{T-243}{1000}. \tag{2}$$

ρ_i and ρ_r are the grain density of ice and rock, respectively, and T is the material temperature in Kelvin. We assume that ρ_i is 920 kg/m^3, ρ_r is 2,500 kg/m^3, and T is 170 K. Variations in these parameters yield relatively small changes in model estimates of ε''. For example, for a mixture of 10% rock and 90% ice, varying T by 10 K causes ε'' to change by 0.01, whereas varying ρ_r by 500 kg/m^3 causes ε'' to change by <0.2. These variations are minor, and the uncertainty in the observational estimates of ε'' inferred from SHARAD data dominates the overall uncertainty. Other formulas for the dielectric permittivity of rock-ice mixtures on Mars have also been considered in previous work (e.g., Lauro et al., 2010).

3. Results

3.1. Mars

In the south polar region of Mars, we identified 31 impact craters that contain CCFDs, 7 impact craters that contain marginal deposits, and 66 impact craters that contain irregular deposits. A map showing the locations of these 104 deposits is shown in Figure 3. The diameters of the CCFD host craters are between 13
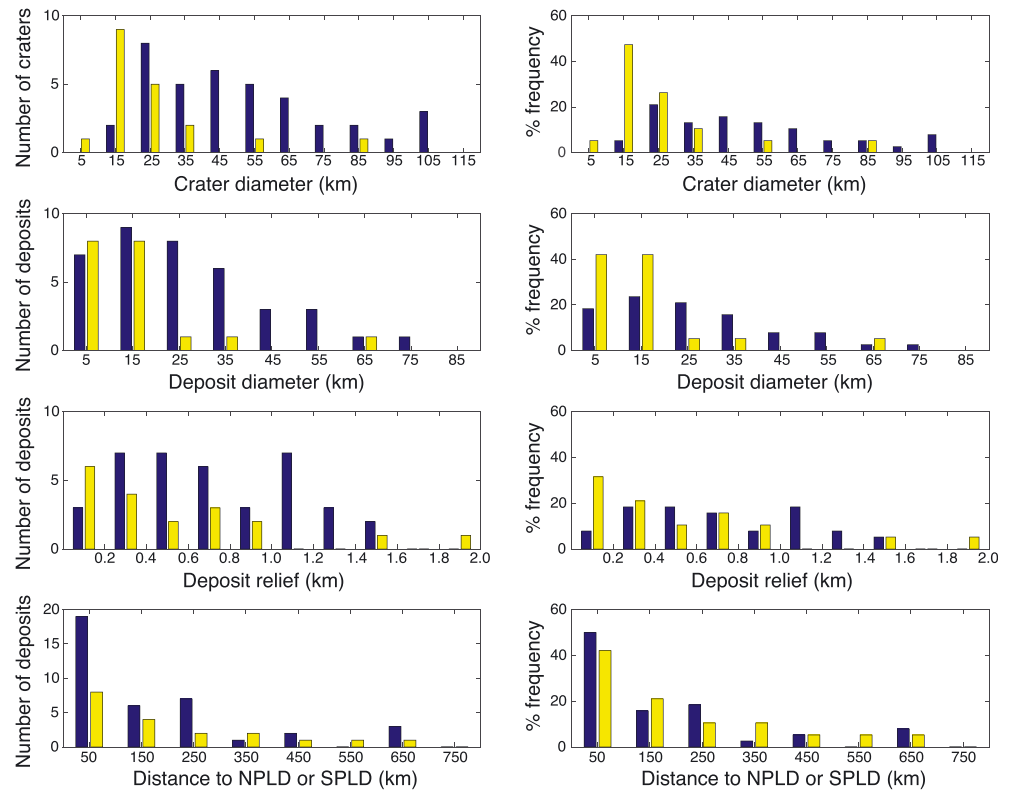
Figure 4. Histograms of crater size for craters that host deposits (first row), deposit diameter (second row), deposit apparent topographic relief (third row), and distance of deposits away from the NPLD or SPLD (fourth row). The left columns are in absolute number of deposits; the right columns are normalized as percentages. Histogram bins have widths of 10 km, 10 km, 200 m, and 100 km for the four rows from top to bottom. Data for north polar crater deposits come from Conway et al. (2012); data for south polar crater deposits are for the 31 circumpolar crater filling deposits and 7 marginal deposits identified here. In all plots, yellow bars represent north polar deposits and blue bars represent south polar deposits. NPLD = north polar layered deposit; SPLD = south polar layered deposit.

and 110 km. The deposits themselves range in diameter from 5 to 74 km, have an apparent topographic relief between 80 and 1,450 m, and are located at distances of up to 690 km from the SPLD. These values are similar to those of ice mounds identified in the north polar region of Mars (Conway et al., 2012). The northern ice mounds are located in craters with diameters between 9 and 83 km, have mound diameters from 5 to 64 km, range in topographic relief from 100 to 1,820 m, and are located at distances of up to 624 km away from the NPLD. The total CCFD volume is between 15,000 and 38,000 km^3, depending on whether the apparent or derived mound thickness is considered. This volume is between 10.4 and 26.3 cm if converted to a global equivalent layer. Some deposits (21 of 31 CCFDs and 5 of 7 marginal deposits) are offset from the crater center by as much as 15 km. Histograms showing the distributions of crater diameter, deposit diameter, deposit relief, and distribution of distances away from the PLD are shown in Figure 4. Data for all 31 CCFDs are recorded in Table 1, and data for all seven marginal deposits are recorded in Table 2. Data for the 66 irregular deposits are provided as supporting information.

HiRISE images were used to catalog the presence of dunes or layering. Partial HiRISE coverage by at least one image occurs for 22 out of 31 CCFDs. Of those 22 CCFDs, 19 were observed to host dunes on their surface, and 12 were observed to have some exposed layering. Examples are shown in Figure 5. Figure 5a shows dunes atop the CCFD in Richardson crater, a dune field that has been previously analyzed (Kereszturi et al., 2011) and is one of the diverse types of dune fields found on Mars (e.g., Chojnacki et al., 2014). Figure 5b shows layers exposed in the CCFD in Burroughs crater, appearing similar to some layering observed in HiRISE images at the NPLD and SPLD (Herkenhoff et al., 2007). Dunes and layering can sometimes be seen in the THEMIS mosaic but are most confidently identified using HiRISE images. We cannot reject

Table 1

Measured Characteristics of CCFDs in the South Polar Region of Mars

ID number	Crater name	Latitude	Longitude	Crater D	Crater d	Deposit D	Deposit H	Offset	Distance to SPLD	Dunes	Layers	Stacked	Margin rim
1	Deseado	−80.64	70.18	25.7	1.46	8.8	0.32	3, WNW	15	Yes	Yes	No	No
2	Jeans	−69.67	154.26	76.6	1.08	44.5	0.37	0	71	Yes	No	No	Yes
3	—	−70.43	158.88	40.2	0.63	21.5	1.32	0	30	Yes	No	No	No
4	—	−68.59	162.67	45.9	0.81	25.7	0.77	11, N	111	Yes	No	No	No
5	—	−67.96	163.1	27.0	0.55	15.2	0.45	6, WNW	148	Yes	No	No	No
6	—	−66.59	161.05	32.9	0.64	18.8	0.54	7, NE	220	Yes	No	No	No
7	—	−66.05	161.59	32.9	0.64	20.8	0.68	4, NE	251	Yes	No	No	No
8	—	−67.88	170.55	38.9	1.26	10.3	0.60	9, SW	235	No	No	No	No
9	Richardson	−72.48	180.21	88.9	0.00	56.0	1.32	0	17	Yes	Yes	No	Yes
10	—	−70.56	178.7	43.8	1.69	25.8	1.10	9, NW	155	Yes	No	No	No
11	—	−74.55	194.13	56.4	1.59	35.3	0.80	0	22	No	Yes	Yes	No
12	—	−75.68	192.75	25.0	0.65	7.7	0.21	0	19	No	No	No	No
13	Reynolds	−75.00	202.45	90.7	2.11	59.5	1.45	0	9	Yes	Yes	Yes	Yes
14	—	−74.13	200.99	87.7	1.85	33.0	0.67	14, SW	23	Yes	Yes	Yes	Yes
15	—	−72.86	204.76	52.9	1.99	26.6	1.07	7, WSW	103	No	Yes	No	No
16	—	−70.86	216.59	50.1	1.29	19.3	0.63	3, S	223	Yes	No	No	No
17	—	−78.95	228.77	45.9	1.09	27.8	0.77	0	5	No	Yes	Yes	Yes
18	Playfair	−77.87	234.36	62.2	1.57	37.0	0.92	0	75	Yes	Yes	Yes	No
19	—	−73.23	224.78	64.8	1.64	27.5	0.44	7, WSW	177	Yes	Yes	No	No
20	—	−70.91	229.24	75.2	1.97	28.0	1.03	15, NNW	338	No	No	No	Yes
21	—	−65.52	235.77	18.6	0.94	8.5	0.83	3, SW	681	Yes	No	No	No
22	—	−66.26	242.55	39.9	2.78	13.2	0.51	0	690	No	No	No	No
23	—	−75.16	254.12	24.5	0.77	19.0	0.08	0	239	No	No	No	No
24	South	−76.91	21.79	101.9	1.85	62.0	1.18	7, NW	77	Yes	Yes	Yes	Yes
25	Burroughs	−72.27	116.62	109.5	2.15	73.5	0.60	4, W	236	Yes	Yes	No	No
26	—	−66.18	151.49	42.7	0.43	11.0	0.40	6, NW	274	Yes	No	No	Yes
27	—	−64.54	158.56	37.0	1.86	15.5	1.11	6, NW	405	Yes	No	No	No
28	Agassiz	−69.86	271.18	108.8	1.84	43.0	0.36	9, SW	604	No	No	No	No
29	—	−64.01	156.16	22.2	0.39	8.0	0.23	4, SSW	419	No	No	No	No
30	—	−68.82	139.73	13.5	0.62	5.8	0.41	3, NW	164	No	No	No	No
31	—	−73.13	181.92	59.8	1.43	34.5	1.13	8, SE	11	No	Yes	No	No

Note. Latitude is in degrees north, longitude is in degrees east, and all other measurements are in kilometers. D is diameter, d is apparent depth, and H is apparent mound relief. Offset measures the distance and direction between the center of the deposit and the center of the crater. CCFD = circumpolar crater filling deposit; SPLD = south polar layered deposit.

the possibility that full HiRISE coverage of all CCFDs would show that they all contain dunes and layers, and so these results are best interpreted as lower limits.

MOLA topography was used to categorize certain morphologic properties of the CCFDs. Of the 31 CCFDs, six were found to have a morphology that appeared "stacked." These six features had characteristic convex, mound-shaped morphology that superposed a lower part of the deposit that was typically flatter. South

Table 2

Measured Characteristics of Marginal Deposits in the South Polar Region of Mars

ID number	Crater name	Latitude	Longitude	Crater D	Crater d	Deposit D	Deposit H	Offset
32	Elim	−80.14	96.86	44.3	1.06	30.3	1.25	4, SSW
33	—	−79.56	117.14	23.0	0.70	10.7	0.36	3, WNW
34	—	−74.87	187.28	67.3	1.55	46.5	1.46	7, WSW
35	—	−75.59	213.23	20.2	0.51	5.5	0.16	5, WSW
36	—	−76.35	215.06	20.2	0.51	6.5	0.14	4, W
37	—	−78.51	216.90	68.8	1.15	52.0	1.07	0
38	—	−79.58	235.85	54.3	1.20	35.0	0.83	0

Note. Latitude is in degrees north, longitude is in degrees east, and all other measurements are in kilometers. D is diameter, d is depth, and H is topographic relief. Offset measures the distance and direction between the center of the deposit and the center of the crater
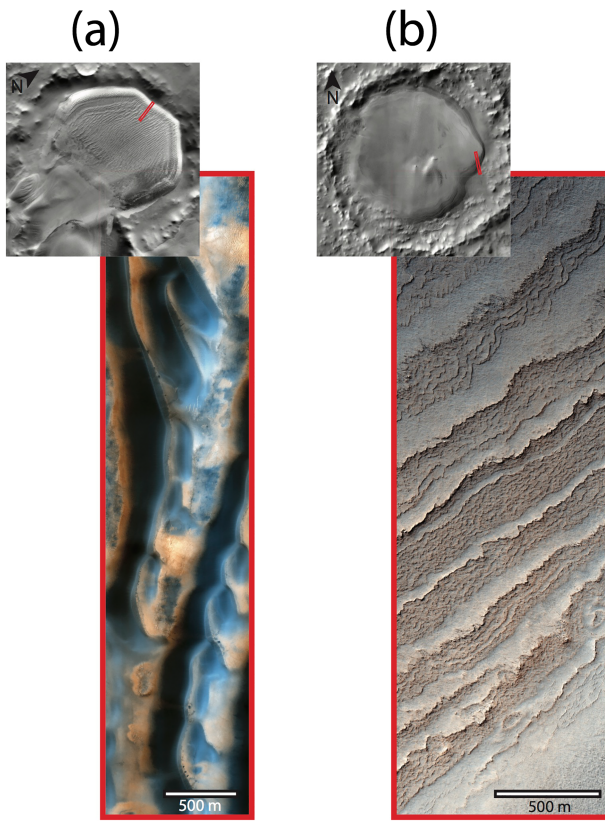
Figure 5. High Resolution Imaging Science Experiment (HiRISE) images of circumpolar crater filling deposits (CCFDs), shown as insets in daytime Thermal Emission Imaging System infrared mosaics. (a) Enhanced color portion of HiRISE image ESP_031749_1080 showing dunes on the CCFD in Richardson crater (89-km crater diameter, 72.5°S, 180.2°E). (b) Enhanced color portion of HiRISE image ESP_057439_1075 showing layer exposures of the CCFD in Burroughs crater (110-km crater diameter, 72.3°S, 116.6°E). The HiRISE image scale bars are 500 m in length.

crater, shown in Figure 2b, is one such example. Of the 31 CCFDs, eight were observed to have an upraised rim (distinct from the crater's rim) that partially encircled the deposit at its margin. The unnamed crater shown in Figure 2a is one such example. We only identified stacking and margin rims if they were apparent in MOLA topography. It is possible that higher-resolution topography would reveal that stacking or margin rims are present at other CCFDs. As with dunes and layers, the numbers here are best interpreted as lower limits.

We considered SHARAD radargrams for four deposits. These four instances were chosen because the radargram passed near the center of the deposit and HRSC DEMs that covered the entirety of the crater were available (the DEM and radargram numbers are given in the supporting information). One radargram, for the CCFD in Reynolds Crater, contains a subsurface reflector that does not appear in the clutter simulation; this example is shown in Figure 6. The SHARAD track identification number is s00266001, and the HRSC DEM identification number is H2179_0000_DT4. We interpreted this subsurface reflector as representing the interface between the base of the CCFD and the underlying crater floor. Under this assumption, the inferred real component of the dielectric permittivity for this CCFD is between 2.6 and 7.8. The range considers a lower and upper bound for deposit thickness of 1.5 and 2.6 km, depending on the method used (see section 2.1).

3.2. Pluto

On Pluto, we found five bright albedo features in craters that are near but separate from Sputnik Planitia. These features are mapped in Figure 7. These bright albedo features have corresponding spectroscopic detections of N_2 (Grundy et al., 2016) and are interpreted in geologic mapping as "shallow N_2 ice" (White et al., 2017). We therefore identified these features outlying the main Sputnik Planitia deposit as N_2 ice. The hosting crater diameters range from 18 to 79 km and are located at distances of 94–325 km from Sputnik Planitia (Table 3). Four of the five features do not have an obvious topographic signature. The fifth bright albedo feature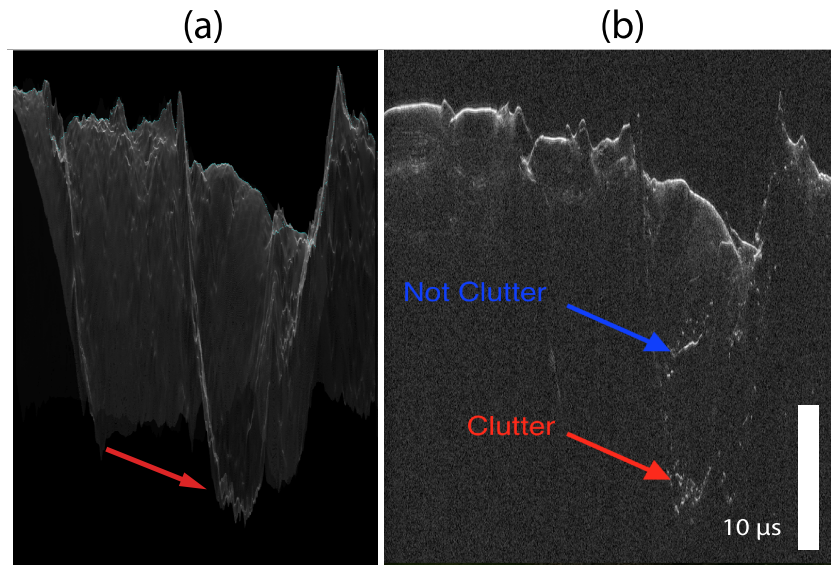, however, does have observable topography, and we consider it further (Figure 7 inset). For ease of referencing in the remainder of the text, we informally refer to it as "Blue Devil crater".

The N_2 ice feature in Blue Devil crater has remarkably similar topography to some Martian ice mounds (e.g., Figure 1b). The topography is convex, offset from the crater center, and does not fill the entire crater floor. The feature is up to 160 m thick, which may be a lower limit given the spatial resolution of the data. Other potential explanations for the topography are unlikely. The dome is too broad and off-center to be the central peak of a complex crater. It is unlikely to represent updoming from viscous relaxation because the crater's "bedrock" of H_2O does not appreciably flow at Pluto's temperatures for relevant geological timescales (e.g., Howard et al., 2017). Finally, the crater is too large for the impact that formed the crater to be in the "strength regime" (Melosh, 1989) where domes or pits may form as a result of target layering. Therefore, we conclude the most likely explanation is that Blue Devil crater hosts an N_2 ice mound analogous to the H_2O ice mounds on Mars.

In addition, we searched for convex topographic mounds within all craters >20 km in diameter within 500 km of Sputnik Planitia that do not contain any anomalously bright deposits in New Horizons images. We found that none of these craters had clear topographic signatures analogous to the Martian ice mounds. Vertical precision in the New Horizons-derived topographic map is typically hundreds of meters (Schenk et al., 2018), so this result is best interpreted as evidence that there are no dark, convex outlying ice deposits near Sputnik Planitia that are 400 m or greater in thickness.

(a)   (b)

Figure 6. Radar track and corresponding clutter simulation for the circumpolar crater filling deposit in Reynolds crater. (a) High Resolution Stereo Camera clutter simulation of Shallow Radar radargram s00266001. (b) Shallow Radar radargram s00266001, which passes through the circumpolar crater filling deposit in Reynolds crater. Labeled in red is a feature interpreted as clutter, and labeled in blue is a feature interpreted to represent a subsurface reflector.

4. Discussion

4.1. CCFD Composition

We argue that the compositional explanation most consistent with the measurements and analysis described in section 3 is that the CCFDs near the south pole of Mars are primarily composed of water ice. Lines of reasoning described below supporting this interpretation include their spatial distribution, morphological arguments, similarity to marginal deposits, radar analysis, and features seen in HiRISE images. None of these factors alone prove that the CCFDs are water ice, but collectively, they support an H_2O composition as most likely.

Perhaps the simplest line of evidence for a volatile composition of the CCFDs comes from their location and distribution. The CCFDs identified here exist at southern polar latitudes, where under the current orbital
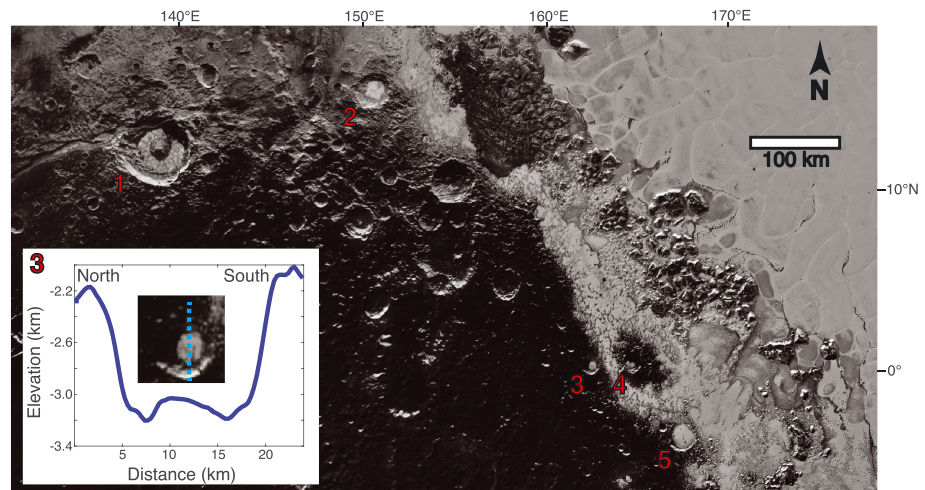

Figure 7. Map of five outliers of N_2 ice within impact craters on Pluto. Labels are to the lower left of each crater on a Long-Range Reconnaissance Imager image mosaic. Inset shows a north-south topographic profile through the N_2 ice in Blue Devil crater (Label 3 on the map) and an enlarged image of that crater with the location of the extracted topographic profile marked with a dashed cyan line. Topography data come from New Horizons stereo images (Schenk et al., 2018).

Table 3
Measured characteristics of Ice Outliers on Pluto and Their Host Craters

ID number	Crater name	Latitude	Longitude	Crater D	Crater d	Derived crater d	Ice D	Ice H	Distance to SP	Notes
1	Elliot	12.0	139.0	79	3.5	1.7–4.2	49	—	325	Annulus shape; inner D = 23 km
2	—	15.2	150.7	39	2.2	1.1–2.8	20	—	94	—
3	—	0.3	162.4	18	0.9	0.6–1.8	9	0.2	170	—
4	—	0.4	164.7	22	1.5	0.7–2.1	8	—	144	—
5	—	-3.5	167.5	33	0.8	1.0–2.6	26	—	151	—

Note. Latitude is in degrees north, longitude is in degrees east, and all other measurements are in kilometers. D is diameter, d is depth, H is topographic relief, and SP is Sputnik Planitia.

configuration of Mars ice is stable at the surface or very near the surface beneath a thin millimeter-to-centimeter-scale protective layer of lag (Schorghofer & Aharonson, 2005). In Figure 8, the volume of each CCFD is plotted as a function of distance from the SPLD. There is a negative trend, as deposits tend to become less voluminous the farther away they are from the SPLD. This trend may reflect decreasing volatile stability away from the SPLD. Finally, the marginal deposits are likely composed of the same material as the SPLD by virtue of their continuous nature with the SPLD. Therefore, if CCFDs and marginal deposits represent the same type of features, the CCFDs are also likely composed of material similar to the SPLD. The SPLD has been shown to be composed primarily of H_2O ice on the basis of rheological arguments that rejected CO_2 ice as the primary constituent (Nye, 2000), gravity analysis that was consistent with a composition of 85% H_2O ice and 15% dust (Zuber et al., 2007; Wieczorek, 2008), and radar analysis that implied a nearly pure H_2O ice composition (Picardi et al., 2005; Plaut et al., 2007).

Extensive morphological similarities between the CCFDs identified here and the northern ice mounds identified by Conway et al. (2012) suggest that they may be composed of the same material. As shown in Figures 4 and 5, the CCFDs have similar sizes, topographic relief, and host-crater properties as the ice mounds in the north polar region. We caution the reader that morphological similarity alone is not sufficient to prove that two features have the same composition, as there are crater fill deposits elsewhere on Mars that have reasonably similar shapes to the CCFDs but are not composed of water ice (e.g., Andrews-Hanna et al., 2010; Bennett & Bell, 2016). Morphological criteria must be interpreted in conjunction with other lines of evidence to infer composition.
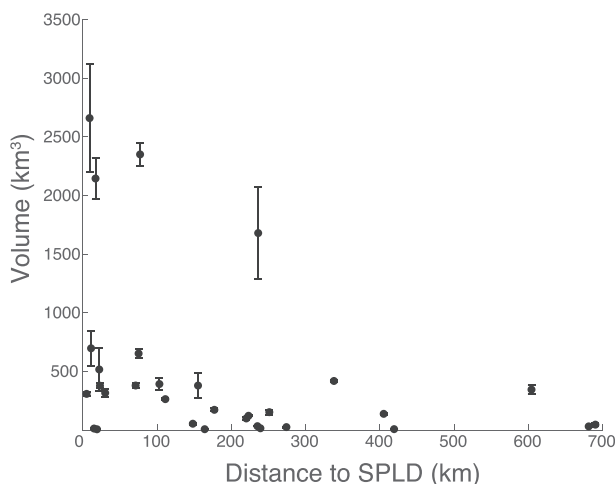

Figure 8. Volumes of the 31 circumpolar crater filling deposits near the south pole of Mars as a function of their distance from the SPLD (volumes assume "apparent deposit relief" for each circumpolar crater filling deposit as defined in section 2.1; error bars represent uncertainties defined in section 2.1). SPLD = south polar layered deposit.

One way to directly constrain composition is through radar analysis. Unfortunately, HRSC DEMs only cover a few CCFD-hosting craters. The SHARAD-derived value of ε' for the deposit in Reynolds Crater with a clearly visible, nonclutter subsurface reflector (Figure 6) is between 2.6 and 7.8. This range encompasses the ε' of H_2O ice (Matsuoka et al., 1997) and of 90% H_2O ice mixed with 10% rock, an upper limit on the silicate dust content of the SPLD (Plaut et al., 2007). The ε' of pure ice is 3.15, the ε' of the ice-rock mixture is 3.49 when considering the mixing model of Stillman et al. (2010), and the ε' of the ice-rock mixture is 3.86 when considering the mixing model of Brouet et al. (2019). Pure ice with 10% porosity has ε' of 2.86 or 2.61, considering the mixing model of Stillman et al. (2010) and Brouet et al. (2019), respectively. A mixture of 80% ice, 10% rock, and 10% porosity has ε' of 3.18 or 3.45, considering the mixing model of Stillman et al. (2010) and Brouet et al. (2019), respectively. Of course, the observed estimate of between 2.6 and 7.8 also encompasses our assumed ε' of pure rock, 7.54. Thus, the range of plausible ε' is large and does not uniquely map to composition (e.g., Bramson et al., 2015), but the SHARAD analysis at least allows for a primarily icy composition that is similar to the SPLD. As expected, we do not observe any bright basal reflections that could be indicative of basal melt (Orosei et al., 2018), because none of the deposits are thick enough to sufficiently
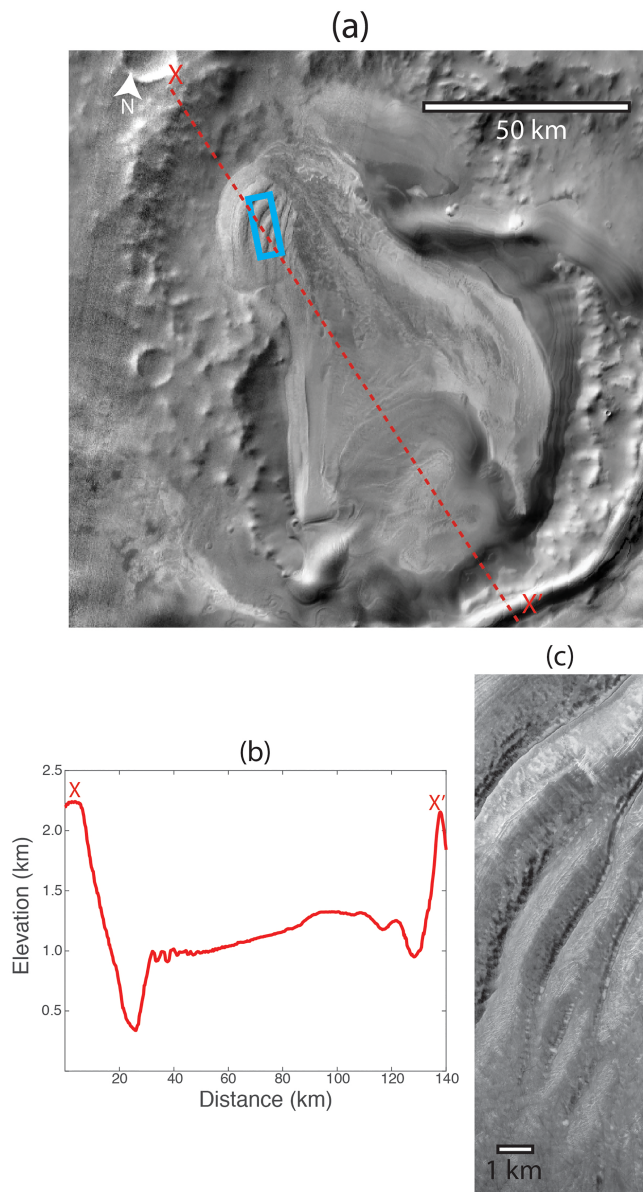
Figure 9. (a) Daytime Thermal Emission Imaging System infrared mosaic of circumpolar crater filling deposit (CCFD) in Reynolds crater at 75.0°S, 202.5°E, flowing into another CCFD in an unnamed crater. (b) Topographic profile from Mars Orbiter Laser Altimeter topography across both CCFDs, represented by the red dashed line in (a). (c) High Resolution Imaging Science Experiment image ESP_013169_1055 showing ridges at the terminus of the flow, represented by the blue rectangle in (a).

heat up their base without a local geothermal heat anomaly (Sori & Bramson, 2019).

Some CCFDs exhibit a morphology that suggests viscous flow. The strongest example is in Reynolds crater, where the CCFD appears to have flowed into another crater (Figure 9). The deposit has contiguous material between the centers of two craters (ID numbers 13 and 14 in Table 1) and ridges at one boundary of the deposit. The ridges do not have the morphology or color of dunes we observed on CCFDs (e.g., Figure 5a). Instead, these ridges may be compressional features where the material pushed up against the second crater's wall, a possibility that requires flow. Therefore, if this interpretation is correct, the CCFD's morphology is inconsistent with a composition of only rocky material but is consistent with glacial deformation of ice. Further implications of this flow are discussed in section 4.4. The other craters that exhibit similar features that might be suggestive of flow, but are not as strong of cases as Reynolds crater, are craters 9, 24, and 31 (ID numbers in Table 1).

We inspected the colorized global mosaic (resolution 231 m/pixel at the equator) of the Mars Digital Image Model created from Viking Orbiter data and found that none of the CCFDs identified here have perennially bright albedo, as observed for some ice mounds in the north polar region (e.g., Bapst et al., 2018). Thus, we cannot confidently state that southern CCFDs have broad exposures of H_2O ice observable at their surface. We do not consider this result contradictory with our interpretation of an icy composition, as surface layers do not necessarily reflect composition at depth. While some northern mounds do contain clear exposures of H_2O (Bapst et al., 2018; Brown et al., 2008; Conway et al., 2012), hemispherical differences are not surprising given large differences in elevation (~5 km). The vast majority of the NPLD surface is exposed H_2O ice, while most of the SPLD surface is not. The same relationship seems to hold true for the northern versus southern crater deposits, where the vast majority of all ice in the south polar region is covered by darker material.

4.2. Formation Mechanisms

Because we find many CCFDs, we consider deposit formation mechanisms that invoke effects of the host crater topography in the preservation or accumulation of ice or that invoke the impact process in the origin of the ice. We consider mechanisms proposed for ice mounds in the north polar region (Conway et al., 2012). These mechanisms include preferential accumulation of ice within polar craters, preferential preservation of an old ice sheet within polar craters, and activation of a hydrothermal system as a result of the impact process. We note that these mechanisms are fundamentally different from those of ice deposits that exist in polar craters on airless bodies, where permanent shadowing without an atmosphere allows some crater floors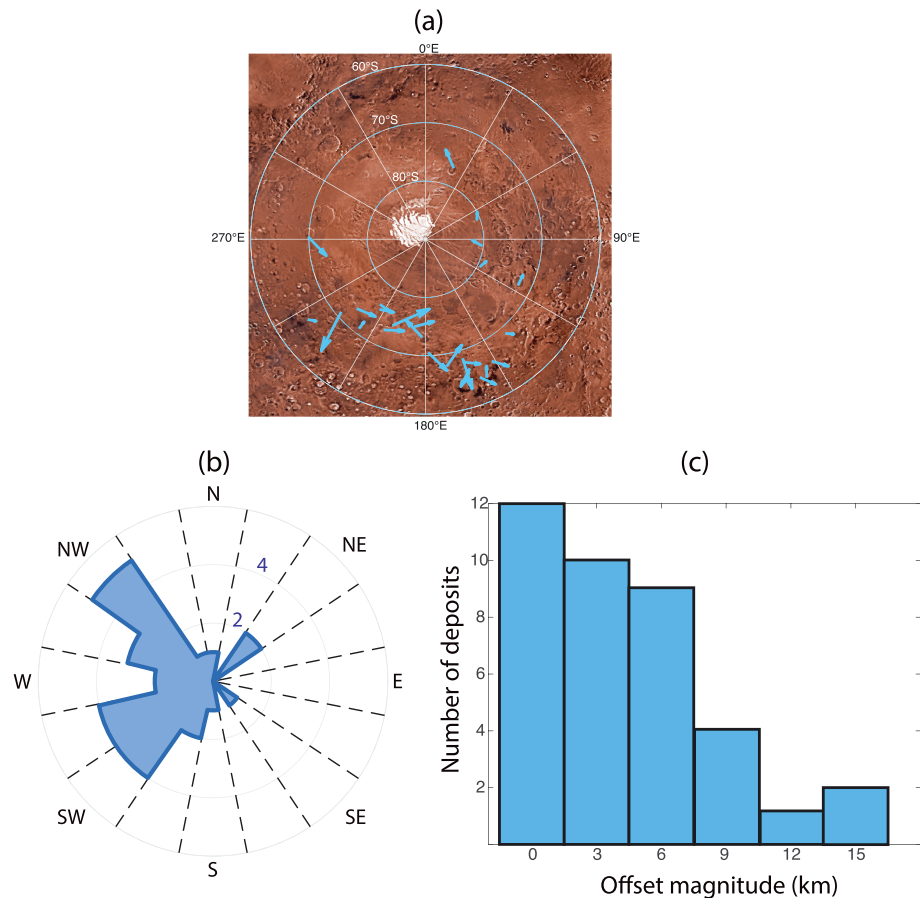 to be cold enough to retain ices over billion year timescales on the Moon (e.g., Nozette et al., 2001), Mercury (e.g., Slade et al., 1992), and Ceres (e.g., Platz et al., 2016).

The locations of CCFDs, both in the regional setting of the south polar region and the local setting of the host crater floor, elucidate their origins. Regionally, the CCFDs are concentrated within a specific range of longitudes. Greater than 90% of all CCFDs (28 of 31) are located within <40% of all longitudes (139–272°E), a configuration that has less than a one-in-a-million probability of occurring by chance if mounds were to form uniformly with longitude. This trend may be partly explained by a heterogeneity in crater density with longitude but not entirely: For example, longitudes between 60° and 120°E are heavily cratered between latitudes 60°S and 80°S but have a dearth of CCFDs. This trend is inconsistent with activation of hydrothermal

Figure 10. (a) Map of directions and magnitudes of the offset between the center of a circumpolar crater filling deposit (CCFD) or marginal deposit relative to the center of the deposit's hosting crater. The longest arrow represents an offset of 15 km. (b) Rose diagram showing a histogram of offset directions. The 10 CCFDs and 2 marginal deposits with no detectable offsets are not mapped or plotted here. (c) Histogram of the magnitude of the offsets for all 38 CCFDs and marginal deposits.

systems from the impact process, which would instead predict that CCFD formation occurs uniformly in heavily cratered terrain so long as groundwater or ice is present. Because near-surface hydrogen is indeed found to be abundant at polar latitudes for all longitudes (Feldman et al., 2004), we reject impact activation of hydrothermal systems as a mechanism for CCFD formation.

Locally, most southern CCFDs are not observed to have centers that exactly coincide with that of their host craters, a property also true for northern CCFDs (Conway et al., 2012). Out of 31 CCFDs, 21 are found to be off-center by >2 km (Table 1), as are 5 of 7 marginal deposits (Table 2). The magnitudes and directions of the offsets are plotted in Figure 10a. A histogram of the offset directions and magnitudes is shown in Figures 10b and 10c, respectively. Out of 26 deposits with offsets, 21 are offset to the west of the crater center. The probability of 21 or more offsets occurring in a particular cardinal direction at random is <1%. We thus interpret the offset directions as indicative of some characteristic of CCFD formation and/or evolution.

Offset directions are inconsistent with insolation as the dominant factor in controlling deposit morphology. If insolation alone determined ice growth, we would expect accumulation to occur preferentially on colder, poleward-facing slopes and for deposits to display a trend of being offset to the south. Alternatively, if ice mounds formed from another mechanism but insolation was the dominant factor in preferential sublimation of the mound, we would expect preferential sublimation on warmer equatorward-facing slopes, and the deposits may instead display a trend of being offset to the north. While insolation is likely to be important for any accumulation or preservation of ice on Mars, it cannot be the only factor at play here.

Offset directions are instead consistent with wind. Basic physical arguments, mesoscale atmospheric models, and geomorphological observations (e.g., Smith et al., 2015) predict deflection of winds emanating from the south pole by the Coriolis Force. Such deflection results in a general westward trend of winds (i.e., easterlies) in the south polar regions outside the SPLD, matching the CCFDs offsets we observe. This correlation implies that wind is important in CCFD formation and/or evolution. For the case where winds control CCFD formation, katabatic winds may travel down the east side of crater walls and preferentially deposit ice on the west side of the crater via orographic precipitation as they flow up the west crater wall. This mechanism thus favors local accumulation of ice within craters, forming as outliers to the SPLD. Alternatively, if a large ice sheet once existed over the locations of all current CCFDs (i.e., a formerly more extensive SPLD), remnants of that ice sheet within craters may be preferentially eroded by wind into their current westward positions. A similar mechanism has been proposed for sedimentary deposits at low Martian latitudes (Bennett & Bell, 2016; Steele et al., 2018). Some role for local accumulation is likely required to form ice mounds near the north pole (Conway et al., 2012), but this process does not necessarily reject the hypothesis that the cores of the deposits come from a formerly more extensive ice sheet. Quantitative signal matching between layer properties in the ice mounds and layer properties in the PLDs will be useful to test whether the ice mounds contain a unique paleoclimate record and thus are not sourced from an older NPLD or SPLD.

Whatever the formation mechanism, the stacked morphology observed in six CCFDs may represent multiple episodes of accumulation. This characteristic is only observed in deposits near the SPLD, with the most distant stacked CCFD 77 km away (compared to 690 km for the most distant CCFD in general and 719 km for the most distant irregular deposit). This proximity suggests either that ice deposition is more frequent in craters near the SPLD or that some episodes of accumulation that have occurred in distant craters are no longer recorded in the present-day geology of those craters.

4.3. Irregular Deposits

The 66 irregular deposits have thus far been excluded from our analysis. Because of their varied morphology and generally smaller size (which makes SHARAD analysis more difficult), we cannot confidently argue for a primarily icy composition from observational evidence. While we cannot be certain these irregular deposits are analogous to ice mounds in the north polar region, we still measure their locations, offsets from their crater centers, and distances to the SPLD. This information is provided as supporting information, including plots showing the distribution of host crater diameter and distance away from the SPLD (Figure S2) and the distribution of the directions and magnitudes of the offsets (Figure S3).

Some of the irregular deposits may represent dune fields. Indeed, many of the irregular deposits we identify are labeled as dunes in the Mars Global Digital Dune Database (Hayward et al., 2014). However, dunes and icy CCFDs are not mutually exclusive. Most ice mounds in the north polar region have at least partial dune cover, and Conway et al. (2012) argue that the completely dune-covered mounds may also contain an ice core. It is possible that the same phenomenon occurs in the south polar region and that some irregular deposits represent dunes overlaying cohesive icy material, which we propose occurs in some of the CCFDs as well (e.g., Richardson crater). It has been suggested that ice may act as an indurating agent, rendering dunes immobile (Fenton & Hayward, 2010). A possibility for formation would then be that irregular deposits represent the remnants of old CCFDs that experienced substantial sublimation until lag cover or dune material thermally protected the remaining ice from complete disappearance (e.g., Bramson et al., 2017). Ultimately, more abundant high-resolution images and topography over the irregular deposits may be required to investigate this possibility further.

4.4. Implications for the PLD

The layering exposed in some CCFDs represents a paleoclimate proxy that may have important implications for the climate record of the SPLD. If the CCFDs represent a formerly larger SPLD, their locations can be used to map the SPLD's former extent, and their climate records may be ancient. Alternatively, the CCFDs may represent isolated, local accumulation in which case their layer exposures could represent a young record that might not be decipherable in SPLD exposures. An intermediate case is that the CCFDs layers are equivalent to one of three distinct stratigraphic units proposed in the SPLD that represent different periods of accumulation (Becerra et al., 2019; Milkovich & Plaut, 2008). Future work may use tools such as stratigraphic analysis (Becerra et al., 2016), wavelet analysis (Becerra et al., 2017; Perron & Huybers, 2009), and

dynamic time warping (Sori et al., 2014) to determine which, if any, of these hypotheses are correct. Layer exposures such as those visible in the HiRISE image shown in Figure 5b are especially promising sites for future analysis because they apparently display multiple periodicities in their stratigraphy, a property necessary to tie the stratigraphy to orbital cycles. However, local topography will be needed to confirm this attribute for this particular site, and it is worth noting that different CCFDs may not all hold the same paleoclimate record.

Another implication of CCFDs for the evolution of the PLDs concerns glacial flow. The importance of viscous flow in the polar regions of Mars has been a topic of debate. It has been argued that the morphology of large portions of the NPLD resembles a flowing ice mass (Winebrenner et al., 2008), and some numerical modeling studies have predicted that viscous flow should be an important process in PLD evolution (Pathare & Paige, 2005). However, SHARAD data have revealed that the NPLD's internal stratigraphy is not consistent with ice flow, as observed radar reflectors do not exhibit dips toward the surface as predicted by flow models (Karlsson et al., 2011). A proposed solution to this inconsistency is that dust-rich layers in both PLDs effectively break up the large ice mass into smaller portions, preventing interior viscous deformation of the stratigraphy (Smith, 2017).

The idea that dusty layers completely prohibit viscous flow of PLD ice is inconsistent with our observations here. Some CCFDs show evidence for flow. Most strongly, as mentioned in section 4.1, the CCFD located in Reynolds crater is layered and exhibits a morphology that suggests that some viscous flow has occurred (Figure 9). This CCFD appears to have flowed into a second crater, showing terminal ridges, a lobate form, and movement away from the south pole. It is possible that layers of dusty ice may hinder glacial flow, but they are not sufficient to prevent it entirely under all conditions. This observation does not imply that the large-scale form of the SPLD is primarily shaped by glacial flow, as other more dominant processes likely occur on shorter timescales (Byrne & Ivanov, 2004). However, localized flow of SPLD ice could be possible under favorable conditions, as predicted for certain young features at the margins of the NPLD (Sori et al., 2016).

4.5. Pluto

The five bright albedo features on Pluto are observed to be outlier N_2 ice deposits on the basis of spectroscopy (Grundy et al., 2016), but we cannot confirm on the basis of New Horizons data whether they are directly atmospherically deposited into their host craters or are remnants of a previously more extensive Sputnik Planitia-like ice sheet. Observations of a crater near Sputnik Planitia that has been breached by ice suggest that glacial flow may play a role in some ice-crater interactions (Stern, Bagenal, et al., 2015). However, on Mars, some craters appear to have been infilled by glacial flow, while others seem to have had ice directly deposited into them, warning against applying the same interpretation to every case.

The N_2 ice mound in Blue Devil crater may represent a valuable record of paleoclimate. On Mars, H_2O ice mounds hold climate records in their layered stratigraphy (Brothers & Holt, 2016; Brown et al., 2008), but that information has not yet been quantitatively analyzed. In part, this is because the larger PLDs contain more abundant and stratigraphically deeper layer exposures, making the PLDs an easier target for image (e.g., Cutts & Lewis, 1982), topographic (e.g., Becerra et al., 2017), or radar-based (e.g., Putzig et al., 2009) paleoclimate analyses. An important difference on Pluto is that the main deposit, Sputnik Planitia, undergoes convection (McKinnon et al., 2016; Trowbridge et al., 2016). Such convection would destroy, on geologically short timescales, any potential paleoclimate record represented by spatial variations of a non-N_2 component (CH_4 ice, CO ice, or H_2O "dust"). Therefore, in contrast to Mars, outlying deposits on Pluto like that in Blue Devil crater may represent the best icy paleoclimate record that can be observed with remote sensing data.

Why does the N_2 ice in Blue Devil crater have thick, dome-like topography but not the other four outlying features in craters on Pluto? We speculate that the answer lies in mound evolution. On Mars, the dome-like shape of H_2O ice mounds is thought to be controlled by the interaction of ice deposition and ablation, glacial flow, and atmospheric effects such as wind (Conway et al., 2012). Pluto's atmosphere is extremely variable over geologic time, far more so than Mars's atmosphere. Pluto's atmospheric pressure may vary by as much as 5 orders of magnitude in a single Plutonian year (Hansen et al., 2015) and perhaps more over longer timescales when changes in orbital parameters are considered. We hypothesize that domes of N_2 ice form in
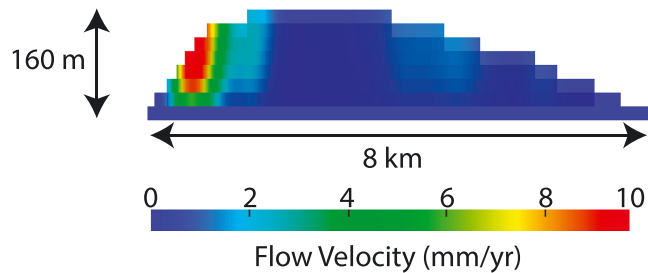
Figure 11. Modeled flow velocities of N_2 ice in the shape of the deposit of Blue Devil crater.

craters on Pluto during times of relatively high atmospheric pressures, but during times of low atmospheric pressure, viscous relaxation becomes the dominant factor in dome evolution without competing atmospheric effects or accumulation, deforming the N_2 ice mounds into flat shapes with unrecognizable topography.

We quantitatively explore this idea using a finite element flow model we have previously developed for icy topography on other planets (Sori et al., 2016), including dome-shaped topography (Sori, Byrne, et al., 2017; Sori et al., 2018). Solving the Stokes equations for conservation of mass and momentum, we calculate flow velocities for an N_2 ice mound with the topographic shape observed in Blue Devil crater overlying immobile bedrock. We use non-Newtonian rheology in which the strain rate of solid, annealed N_2 ice is proportional to the driving stress raised to an exponent of 2.2, as suggested by laboratory experiments (Yamashita et al., 2010) and used in other flow models of Plutonian ice (Umurhan et al., 2017). Our results, shown in Figure 11 for an ice temperature of 45 K, suggest a maximum flow velocity of ~1 cm/year (or ~2.5 m per Pluto year) for Blue Devil crater's ice mound. We emphasize that the rheology of even pure N_2 ice is highly uncertain, and Pluto's features likely have some CO and CH_4 ice mixed in, which could have unknown rheological effects. Therefore, these results are merely approximations, and any following interpretations must take this into account. Nevertheless, we have shown that N_2 ice on Pluto can flow on relatively fast geological timescales, consistent with observations of glacial landforms (Howard et al., 2017). The four outlying N_2 deposits that do not have an obvious convex, dome-like shape in present data may have had their topography subdued by viscous relaxation, and the ice mound in Blue Devil crater could simply be younger than these four, have a higher content of impurities that is sufficient to significantly reduce strain rate, or not be composed primarily of N_2 ice.

One of Pluto's five N_2 ice deposits in outlying craters resides inside Elliot crater (Figure 7, crater Label 1) and has a striking resemblance to a bright albedo feature observed by Voyager 2 on the Uranian moon Umbriel in the crater Wunda. Both the Wunda and Elliot crater features have bright albedos in an annular shape, with a darker "gap" in this annulus (in the case of Elliot crater, this gap may be related to geologically recent cryovolcanism; Cruikshank et al., 2019; Dalle Ore et al., 2019). Previous work (Sori, Bapst, et al., 2017) argued that Wunda's feature was a CO_2 ice deposit on the basis of thermal arguments and volatile migration, with the annular shape the result of volatile deposition inside a complex crater with a central peak. Wunda and Elliot may represent analogous features where volatile stability is favored on the floor of complex craters.

5. Conclusions

We identified deposits within 31 impact craters in the south polar region of Mars that are near to but spatially separated from the SPLD. We conclude that these deposits are primarily composed of water ice on the basis of physical similarities to ice mounds in the north polar region of Mars (Conway et al., 2012), physical similarities to seven crater deposits that are contiguous with the SPLD, radar analysis, and the deposits' spatial distribution. In total, the deposits represent approximately 15,000–38,000 km^3 of solid water. This volume is between 1% and 3% of the volume of the SPLD, a factor of 2–6 times more than the ice volume in north polar ice mounds (Conway et al., 2012), approximately equal to the ice volume found in midlatitude subsurface ice at Arcadia and Utopia Planitia (Bramson et al., 2015; Stuurman et al., 2016), and an order of magnitude less than the ice volume in the collection of midlatitude debris-covered glaciers (Levy et al., 2014). We argue the physical characteristics of the deposits are most directly consistent with wind playing a role in CCFD formation and/or evolution, but we cannot distinguish between the CCFDs forming via local deposition versus being remnants of a formerly more extensive SPLD.

Five deposits of nitrogen ice exist within impact craters on Pluto. Similar to the Mars case, they are near but separated from their planet's large, ~1,000-km-wide ice sheet of the same composition: Sputnik Planitia. The Plutonian data sets do not allow for the same depth of analysis as for Mars, but physical similarities suggest that the features may be analogous to Mars's icy outliers. We conclude that the environment associated with

large impact craters leads to preferential deposition or retention of volatiles and that this phenomenon is not unique to one region or planet.

Several lines of inquiry are promising as the subjects of future work. Observations by the CaSSIS instrument aboard the ExoMars Trace Gas Orbiter can yield high-resolution topography for most (23 of 31) CCFDs, as can further observations by CTX and HiRISE. Paleoclimate analyses using these topographic data sets or image data (Becerra et al., 2016; Sori et al., 2014) may determine whether layering in the CCFDs can be connected with statistical significance to layering of the SPLD, thereby elucidating the climate history of the south polar region. Finally, detailed analysis of the 66 irregular deposits using radar or other data sets can determine whether they too are likely to be partially composed of icy material.

References

Andrews-Hanna, J. C., Zuber, M. T., Arvidson, R. E., & Wiseman, S. M. (2010). Early Mars hydrology: Meridiani playa deposits and the sedimentary record of Arabia Terra. *Journal of Geophysical Research, Planets*, 115, E06002. https://doi.org/10.1029/2009JE003485

Banks, M. E., & Pelletier, J. D. (2008). Forward modeling of ice topography on Mars to infer basal shear stress conditions. *Journal of Geophysical Research*, 113, E01001. https://doi.org/10.1029/2007JE002895

Bapst, J., Byrne, S., & Brown, A. J. (2018). On the icy edge at Louth and Korolev craters. *Icarus*, 308, 15–26. https://doi.org/10.1016/j.icarus.2017.10.004

Becerra, P., Byrne, S., Sori, M. M., Sutton, S., & Herkenhoff, K. E. (2016). Stratigraphy of the north polar layered deposits of Mars from high-resolution topography. *Journal of Geophysical Research: Planets*, 121, 1445–1471. https://doi.org/10.1002/2015JE004992

Becerra, P., Sori, M. M., & Byrne, S. (2017). Signals of astronomical climate forcing in the exposure topography of the North Polar Layered Deposits of Mars. *Geophysical Research Letters*, 44, 62–70. https://doi.org/10.1002/2016GL071197

Becerra, P., Sori, M. M., Thomas, N., Pommerol, A., Simioni, E., Sutton, S. S., et al. (2019). Timescales of the climate record in the south polar ice cap of Mars. *Geophysical Research Letters*, 46(13), 7268–7277. https://doi.org/10.1029/2019GL083588

Bennett, K. A., & Bell, J. F. (2016). A global survey of Martian central mounds: Central mounds as remnants of previously more extensive large-scale sedimentary deposits. *Icarus*, 264, 331–341. https://doi.org/10.1016/j.icarus.2015.09.041

Bramson, A. M., Byrne, S., & Bapst, J. (2017). Preservation of midlatitude ice sheets on Mars. *Journal of Geophysical Research: Planets*, 122, 2250–2266. https://doi.org/10.1002/2017JE005357

Bramson, A. M., Byrne, S., Putzig, N. E., Sutton, S., Plaut, J. J., Brothers, T. C., & Holt, J. W. (2015). Widespread excess ice in Arcadia Planitia, Mars. *Geophysical Research Letters*, 42, 6566–6574. https://doi.org/10.1002/2015GL064844

Brothers, T. C., & Holt, J. W. (2016). Three-dimensional structure and origin of a 1.8 km thick ice dome within Korolev Crater, Mars. *Geophysical Research Letters*, 43, 1443–1449. https://doi.org/10.1002/2015GL066440

Brouet, Y., Becerra, P., Sabouroux, P., Pommerol, A., & Thomas, N. (2019). A laboratory-based dielectric model for the radar sounding of the Martian subsurface. *Icarus*, 321, 960–973. https://doi.org/10.1016/j.icarus.2018.12.029

Brouet, Y., Neves, L., Sabouroux, P., Levasseur-Regourd, A. C., Poch, O., Encrenaz, P., et al. (2016). Characterization of the permittivity of controlled porous water ice-dust mixtures to support the radar exploration of icy bodies. *Journal of Geophysical Research: Planets*, 121, 2426–2443. https://doi.org/10.1002/2016JE005045

Brown, A. J., Byrne, S., Tornabene, L. L., & Roush, T. (2008). Louth crater: Evolution of a layered water ice mound. *Icarus*, 196(2), 433–445. https://doi.org/10.1016/j.icarus.2007.11.023

Byrne, S. (2009). The polar deposits of Mars. *Annual Review of Earth and Planetary Sciences*, 37(1), 535–560. https://doi.org/10.1146/annurev.earth.031208.100101

Byrne, S., & Ivanov, A. B. (2004). Internal structure of the Martian south polar layered deposits. *Journal of Geophysical Research*, 109, E11001. https://doi.org/10.1029/2004JE002267

Campbell, B. A., & Morgan, G. A. (2018). Fine-scale layering of Mars polar deposits and signatures of ice content in nonpolar material from multiband SHARAD data processing. *Geophysical Research Letters*, 45, 1759–1766. https://doi.org/10.1002/2017GL075844

Campbell, M. J., & Ulrichs, J. (1969). Electrical properties of rocks and their significance for lunar radar observations. *Journal of Geophysical Research*, 74, 5867–5881. https://doi.org/10.1029/JB074i025p05867

Chojnacki, M., Burr, D. M., & Moersch, J. E. (2014). Valles Marineris dune fields as compared with other Martian populations: Diversity of dune compositions, morphologies, and thermophysical properties. *Icarus*, 230, 96–142. https://doi.org/10.1016/j.icarus.2013.08.018

Choudhary, P., Holt, J. W., & Kempf, S. D. (2016). Surface clutter and echo location analysis for the interpretation of SHARAD data from Mars. *IEEE Geoscience and Remote Sensing Letters*, 13, 1285–1289. https://doi.org/10.1109/LGRS.2016.2581799

Christensen, P. R., Engle, E., Anwar, S., Dickenshied, S., Noss, D., Gorelick, N., & Weiss-Malik, M. (2009). JMARS—A planetary GIS, Am. Geophys. Union Fall Meeting.

Conway, S. J., Hovius, N., Barnie, T., Besserer, J., Le Mouélic, S., Orosei, R., & Read, N. A. (2012). Climate-driven deposition of water ice and the formation of mounds in craters in Mars' north polar region. *Icarus*, 220, 174–193. https://doi.org/10.1016/j.icarus.2012.04.021

Cruikshank, D. P., Umurhan, O. M., Beyer, R. A., Schmitt, B., Keane, J. T., Runyon, K. D., et al. (2019). Recent cryovolcanism in Virgil Fossae on Pluto. *Icarus*, 330, 155–168. https://doi.org/10.1016/j.icarus.2019.04.023

Cutts, J. A., & Lewis, B. H. (1982). Models of climate cycles recorded in Martian polar layered deposits. *Icarus*, 50(2-3), 216–244. https://doi.org/10.1016/0019-1035(82)90124-5

Dalle Ore, C. M., Cruikshank, D. P., Protopapa, S., Scipioni, F., McKinnon, W. B., Cook, J. C., et al. (2019). Detection of ammonia on Pluto's surface in a region of geologically recent tectonism. *Science Advances*, 5(5), eaav5731. https://doi.org/10.1126/sciadv.aav5731

Edwards, C. S., Nowicki, K. J., Christensen, P. R., Hill, J., Gorelick, N., & Murray, K. (2011). Mosaicking of global planetary image data sets: 1. Techniques and data processing for Thermal Emission Imaging System (THEMIS) multi-spectral data. *Journal of Geophysical Research*, 116, E10008. https://doi.org/10.1029/2010JE003755

Feldman, W. C., Prettyman, T. H., Maurice, S., Plaut, J. J., Bish, D. L., Vaniman, D. T., et al. (2004). Global distribution of near-surface hydrogen on Mars. *Journal of Geophysical Research*, 109, E09006. https://doi.org/10.1029/2003JE002160

Fenton, L. K., & Hayward, R. K. (2010). Southern high latitude dune fields on Mars: Morphology, aeolian inactivity, and climate change. *Geomorphology*, 121, 98–121. https://doi.org/10.1016/j.geomorph.2009.11.006

Garvin, J. B., Sakimoto, S. E. H., Frawley, J. J., & Schnetzler, C. (2000). North polar region crater forms on Mars: Geometric characteristics from the Mars Orbiter Laser Altimeter. *Icarus*, *144*, 329–352. https://doi.org/10.1006/icar.1999.6298

Gladstone, G. R., Stern, S. A., Ennico, K., Olkin, C. B., Weaver, H. A., Young, L. A., et al. (2016). The atmosphere of Pluto as observed by New Horizons. *Science*, *351*, aad8866. https://doi.org/10.1126/science.aad8866

Grundy, W. M., Binzel, R. P., Buratti, B. J., Cook, J. C., Cruikshank, D. P., Dalle Ore, C. M., et al., & and the New Horizons Science Team (2016). Surface compositions across Pluto and Charon. *Science*, *351*, aad9189. https://doi.org/10.1126/science.aad9189

Hansen, C. J., Paige, D. A., & Young, L. A. (2015). Pluto's climate modeled with new observational constraints. *Icarus*, *246*, 183–191. https://doi.org/10.1016/j.icarus.2014.03.014

Hayward, R. K., Fenton, L. K., & Titus, T. N. (2014). Mars Global Digital Dune Database (MGD^3): Global dune distribution and wind pattern observations. *Icarus*, *230*, 38–46. https://doi.org/10.1016/j.icarus.2013.04.011

Herkenhoff, K. E., Byrne, S., Russell, P. S., Fishbaugh, K. E., & McEwen, A. S. (2007). Meter-scale morphology of the north polar region of Mars. *Science*, *317*, 1712–1715. https://doi.org/10.1126/science.1143544

Holt, J. W., Peters, M. E., Kempf, S. D., Morse, D. L., & Blankenship, D. D. (2006). Echo source discrimination in single-pass airborne radar sounding data from the Dry Valleys, Antarctica: Implications for orbital sounding of Mars. *Journal of Geophysical Research*, *111*, E06S24. https://doi.org/10.1029/2005JE002525

Howard, A. D., Moore, J. M., Umurhan, O. M., White, O. L., Anderson, R. S., McKinnon, W. B., et al. (2017). Present and past glaciation on Pluto. *Icarus*, *287*, 287–300. https://doi.org/10.1016/j.icarus.2016.07.006

Karlsson, N. B., Holt, J. W., & Hindmarsh, R. C. A. (2011). Testing for flow in the north polar layered deposits of Mars using radar stratigraphy and a simple 3D ice-flow model. *Geophysical Research Letters*, *38*, L24202. https://doi.org/10.1029/2011GL049630

Keane, J. T., Matsuyama, I., Kamata, S., & Steckloff, J. K. (2016). Reorientation and faulting of Pluto due to volatile loading with Sputnik Planitia. *Nature*, *540*(7631), 90–93. https://doi.org/10.1038/nature20120

Kereszturi, A., Vincendon, M., & Schmidt, F. (2011). Water ice in the dark dune spots of Richardson crater on Mars. *Planetary and Space Science*, *59*(1), 26–42. https://doi.org/10.1016/j.pss.2010.10.015

Kjær, K. H., Larsen, N. K., Binder, T., Bjørk, A. A., Eisen, O., Fahnestock, M. A., et al. (2018). A large impact crater beneath Hiawatha Glacier in northwest Greenland. *Science Advances*, *4*, eaar8173. https://doi.org/10.1126/sciadv.aar8173

Krasilnikov, S. S., Kuzmin, R. O., & Evdokimova, N. A. (2018). Remnant massifs of layered deposits at high northern latitudes of Mars. *Solar System Research*, *52*(1), 26–36. https://doi.org/10.1134/S0038094617060065

Landis, M. E., Byrne, S., Dundas, C. M., Herkenhoff, K. E., Whitten, J. L., Mayer, D. P., et al. (2018). Surface ages of the south polar layered deposits, Mars*, Lunar Planet. Sci. Conf. 49th*, 1605.

Laskar, J., Levrard, B., & Mustard, J. F. (2002). Orbital forcing of the Martian polar layered deposits. *Nature*, *419*, 375–377. https://doi.org/10.1038/nature01066

Lauro, S. E., Mattei, E., Pettinelli, E., Soldovieri, F., Orosei, R., Cartacci, M., et al. (2010). Permittivity estimation of layers beneath the northern polar layered deposits, Mars. *Geophysical Research Letters*, *37*, L14201. https://doi.org/10.1029/2010GL043015

Levy, J. S., Fassett, C. I., Head, J. W., Schwartz, C., & Watters, J. L. (2014). Martian water budget: Geometric constraints on the volume of remnant, midlatitude debris-covered glaciers. *Journal of Geophysical Research: Planets*, *119*, 2188–2196. https://doi.org/10.1002/2014JE004685

Malin, M. C., & Edgett, K. S. (2001). Mars Global Surveyor Mars Orbiter Camera: Interplanetary cruise through primary mission. *Journal of Geophysical Research, Planets*, *106*, 23,429–23,570. https://doi.org/10.1029/2000JE001455

Matsuoka, T., Fujita, S., & Mae, S. (1997). Dielectric properties of ice containing ionic impurities at microwave frequencies. *The Journal of Physical Chemistry. B*, *101*, 6219–6222. https://doi.org/10.1021/jp9631590

McEwen, A. S., Eliason, E. M., Bergstrom, J. W., Bridges, N. T., Hansen, C. J., Delamere, W. A., et al. (2007). Mars Reconnaissance Orbiter's High Resolution Imaging Science Experiment (HiRISE). *Journal of Geophysical Research*, *112*, E05S02. https://doi.org/10.1029/2005JE002605

McKinnon, W. B., Nimmo, F., Wong, T., Schenk, P. M., White, O. L., Roberts, J. H., et al., & the New Horizons Geology, Geophysics and Imaging Theme Team (2016). Convection in a volatile nitrogen-ice-rich layer drives Pluto's geological vigour. *Nature*, *534*(7605), 82–85. https://doi.org/10.1038/nature18289

Melosh, H. J. (1989). *Impact cratering: A geologic process*. Oxford: Oxford University Press.

Milkovich, S. M., & Head, J. W. III (2005). North polar cap of Mars: Polar layered deposit characterization and identification of a fundamental climate signal. *Journal of Geophysical Research*, *110*, E01005. https://doi.org/10.1029/2004JE002349

Milkovich, S. M., & Plaut, J. J. (2008). Martian south polar layered deposit stratigraphy and implications for accumulation history. *Journal of Geophysical Research*, *113*, E06007. https://doi.org/10.1029/2007JE002987

Moore, J. M., McKinnon, W. B., Spencer, J. R., Howard, A. D., Schenk, P. M., Beyer, R. A., et al. (2016). The geology of Pluto and Charon through the eyes of New Horizons. *Science*, *351*(6279), 1284–1293. https://doi.org/10.1126/science.aad7055

Nerozzi, S., & Holt, J. W. (2019). Buried ice and sand caps at the north polar of Mars: Revealing a record of climate change in the cavi unit with SHARAD. *Geophysical Research Letters*, *46*. https://doi.org/10.1029/2019GL082114

Nimmo, F., Hamilton, D. P., McKinnon, W. B., Schenk, P. M., Binzel, R. P., Bierson, C. J., et al., & New Horizons Geology, Geophysics & Imaging Theme Team (2016). Reorientation of Sputnik Planitia implies a subsurface ocean on Pluto. *Nature*, *540*(7631), 94–96. https://doi.org/10.1038/nature20148

Nozette, S., Spudis, P. D., Robinson, M. S., Bussey, D. B. J., Lichtenberg, C., & Bonner, R. (2001). Integration of lunar polar remote-sensing data sets: Evidence for ice at the lunar south pole. *Journal of Geophysical Research, Planets*, *106*, 23,253–23,266. https://doi.org/10.1029/2000JE001417

Nye, J. F. (2000). A flow model for the polar caps of Mars. *Journal of Glaciology*, *46*(154), 438–444. https://doi.org/10.3189/172756500781833151

Olhoeft, G. R. (2003). Electromagnetic field and material properties in ground penetrating radar. In *Proceedings of the 2nd International workshop on advanced ground penetrating radar* (pp. 144–147). Delft, Netherlands. https://doi.org/10.1109/AGPR.2003.1207309

Orosei, R., Lauro, S. E., Pettinelli, E., Cicchetti, A., Coradini, M., Cosciotti, B., et al. (2018). Radar evidence of subglacial liquid water on Mars. *Science*, *361*, eaar7268. https://doi.org/10.1126/science.aar7268

Pathare, A. V., & Paige, D. A. (2005). The effects of Martian orbital variations upon the sublimation and relaxation of north polar troughs and scarps. *Icarus*, *174*, 419–443. https://doi.org/10.1016/j.icarus.2004.10.030

Perron, J. T., & Huybers, P. (2009). Is there an orbital signal in the polar layered deposits on Mars? *Geology*, *37*, 155–158. https://doi.org/10.1130/G25143A.1

Pettinelli, E., Vannaroni,, G., Cereti, A., Pisani, A. R., Paolucci, F., Del Vento, D., et al. (2005). Laboratory investigations into the electromagnetic properties of magnetite/silica mixtures as Martian soil simulants. *Journal of Geophysical Research*, *110*, E04013. https://doi.org/10.1029/2004JE002375

Picardi, G., Plaut, J. J., Biccari, D., Bombaci, O., Calabrese, D., Cartacci, M., et al. (2005). Radar soundings of the subsurface of Mars. *Science*, *310*(5756), 1925–1928. https://doi.org/10.1126/science.1122165

Platz, T., Nathues, A., Schorghofer, N., Preusker, F., Mazarico, E., Schröder, S. E., et al. (2016). Surface water-ice deposits in the northern shadowed regions of Ceres. *Nature Astronomy*, *1*(1), 1–6. https://doi.org/10.1038/s41550-016-0007

Plaut, J. J., Picardi, G., Safaeinili, A., Ivanov, A. B., Milkovich, S. M., Cicchetti, A., et al. (2007). Subsurface radar sounding of the south polar layered deposits of Mars. *Science*, *316*(5821), 92–95. https://doi.org/10.1126/science.1139672

Putzig, N. E., Phillips, R. J., Campbell, B. A., Holt, J. W., Plaut, J. J., Carter, L. M., et al. (2009). Subsurface structure of Planum Boreum from Mars Reconnaissance Orbiter Shallow Radar soundings. *Icarus*, *204*(2), 443–457. https://doi.org/10.1016/j.icarus.2009.07.034

Putzig, N. E., Phillips, R. J., Campbell, B. A., Mellon, M. T., Holt, J. W., & Brothers, T. C. (2014). SHARAD soundings and surface roughness at past, present, and proposed landing sites on Mars: Reflections at Phoenix may be attributable to deep ground ice. *Journal of Geophysical Research: Planets*, *119*, 1936–1949. https://doi.org/10.1002/2014JE004646

Rathbun, J. A., & Squyres, S. W. (2002). Hydrothermal systems associated with Martian impact craters. *Icarus*, *157*(2), 362–372. https://doi.org/10.1006/icar.2002.6838

Robbins, S. J., & Hynek, B. M. (2012). A new global database of Mars impact craters ≥1 km: 1. Database creation, properties, and parameters. *Journal of Geophysical Research*, *117*, E05004. https://doi.org/10.1029/2011JE003966

Russell, P. S., & Head, J. W. III (2002). The Martian hydrosphere/cryosphere system: Implications of the absence of hydrologic activity at Lyot crater. *Geophysical Research Letters*, *29*(17), 1827. https://doi.org/10.1029/2002GL015178

Rust, A. C., Russell, J. K., & Knight, R. J. (1999). Dielectric constant as a predictor of porosity in dry volcanic rocks. *Journal of Volcanology and Geothermal Research*, *91*(1), 79–96. https://doi.org/10.1016/S0377-0273(99)00055-4

Schenk, P. M., Beyer, R. A., McKinnon, W. B., Moore, J. M., Spencer, J. R., White, O. L., et al. (2018). Basins, fractures and volcanoes: Global cartography and topography of Pluto from New Horizons. *Icarus*, *314*, 400–433. https://doi.org/10.1016/j.icarus.2018.06.008

Schorghofer, N., & Aharonson, O. (2005). Stability and exchange of subsurface ice on Mars. *Journal of Geophysical Research*, *110*, E05003. https://doi.org/10.1029/2004JE002350

Seu, R., Phillips, R. J., Biccari, D., Orosei, R., Masdea, A., Picardi, G., et al. (2007). SHARAD sounding radar on the Mars Reconnaissance Orbiter. *Journal of Geophysical Research*, *112*, E09003. https://doi.org/10.1029/2006JE002745

Skinner, J. A., Hare, T. M., & Tanaka, K. L. (2006). Digital renovation of the atlas of Mars 1:15,000,000-scale global geologic series maps, Lunar Planet. Sci. Conf. 37th, 2331.

Slade, M. A., Butler, B. J., & Muhleman, D. O. (1992). Mercury radar imaging: Evidence for polar ice. *Science*, *258*(5082), 635–640. https://doi.org/10.1126/science.258.5082.635

Smith, D. E., Zuber, M. T., Frey, H. V., Garvin, J. B., Head, J. W., Muhleman, D. O., et al. (2001). Mars Orbiter Laser Altimeter: Experiment summary after the first year of global mapping of Mars. *Journal of Geophysical Research*, *106*(E10), 23,689–23,722. https://doi.org/10.1029/2000JE001364

Smith, I. B. (2017). Where ice flows on Mars; Where ice does not seem to flow; Why the difference? Lunar Planet Sci. Conf. 48th, 2489.

Smith, I. B., Spiga, A., & Holt, J. W. (2015). Aeolian processes as drivers of landform evolution at the South Pole of Mars. *Geomorphology*, *240*, 54–69. https://doi.org/10.1016/j.geomorph.2014.08.026

Sori, M. M., Bapst, J., Bramson, A. M., Byrne, S., & Landis, M. E. (2017). A Wunda-full world? Carbon dioxide deposits on Umbriel and other Uranian moons. *Icarus*, *290*, 1–13. https://doi.org/10.1016/j.icarus.2017.02.029

Sori, M. M., & Bramson, A. M. (2019). Water on Mars, with a grain of salt: Local heat anomalies are required for basal melting of ice at the south pole today. *Geophysical Research Letters*, *46*, 1222–1231. https://doi.org/10.1029/2018GL080985

Sori, M. M., Byrne, S., Bland, M. T., Bramson, A. M., Ermakov, A. I., Hamilton, C. W., et al. (2017). The vanishing cryovolcanoes of Ceres. *Geophysical Research Letters*, *44*, 1243–1250. https://doi.org/10.1002/2016GL072319

Sori, M. M., Byrne, S., Hamilton, C. W., & Landis, M. E. (2016). Viscous flow rates of icy topography on the north polar layered deposits of Mars. *Geophysical Research Letters*, *43*, 541–549. https://doi.org/10.1002/2015GL067298

Sori, M. M., Perron, J. T., Huybers, P., & Aharonson, O. (2014). A procedure for testing the significance of orbital tuning of the Martian polar layered deposits. *Icarus*, *235*, 136–146. https://doi.org/10.1016/j.icarus.2014.03.009

Sori, M. M., Sizemore, H. G., Byrne, S., Bramson, A. M., Bland, M. T., Stein, N. T., & Russell, C. T. (2018). Cryovolcanic rates on Ceres revealed by topography. *Nature Astronomy*, *2*, 946–950. https://doi.org/10.1038/s41550-018-0574-1

Steele, L. J., Kite, E. S., & Michaels, T. I. (2018). Crater mound formation by wind erosion on Mars. *Journal of Geophysical Research: Planets*, *123*, 113–130. https://doi.org/10.1002/2017JE005459

Stern, S. A., Bagenal, F., Ennico, K., Gladstone, G. R., Grundy, W. M., McKinnon, W. B., et al. (2015). The Pluto system: Initial results from its exploration by New Horizons. *Science*, *350*, aad1815. https://doi.org/10.1126/science.aad1815

Stern, S. A., Porter, S., & Zangari, A. (2015). On the roles of escape erosion and the viscous relaxation of craters on Pluto. *Icarus*, *250*, 287–293. https://doi.org/10.1016/j.icarus.2014.12.006

Stewart, S. T., & Valiant, G. J. (2006). Martian subsurface properties and crater formation processes inferred from fresh impact crater geometries. *Meteoritics and Planetary Science*, *41*(10), 1509–1537. https://doi.org/10.1111/j.1945-5100.2006.tb00433.x

Stillman, D. E., Grimm, R. E., & Dec, S. F. (2010). Low-frequency electrical properties of ice-silicate mixtures. *The Journal of Physical Chemistry B*, *114*, 6065–6073. https://doi.org/10.1021/jp9070778

Stuurman, C. M., Osinski, G. R., Holt, J. W., Levy, J. S., Brothers, T. C., Kerrigan, M., & Campbell, B. A. (2016). SHARAD detection and characterization of subsurface water ice deposits in Utopia Planitia, Mars. *Geophysical Research Letters*, *43*, 9484–9491. https://doi.org/10.10022/2016GL070138

Tanaka, K. L., & Kolb, E. J. (2001). Geologic history of the polar regions of Mars based on Mars Global Surveyor data. *Icarus*, *154*(1), 3–21. https://doi.org/10.1006/icar.2001.6675

Trowbridge, A. J., Melosh, H. J., Steckloff, J. K., & Freed, A. M. (2016). Vigorous convection as the explanation for Pluto's polygonal terrain. *Nature*, *534*(7605), 79–81. https://doi.org/10.1038/nature18016

Umurhan, O. M., Howard, A. D., Moore, J. M., Earle, A. M., White, O. L., Schenk, P. M., et al. (2017). Modeling glacial flow on and onto Pluto's Sputnik Planitia. *Icarus*, *287*, 301–319. https://doi.org/10.1016/j.icarus.2017.01.017

Westbrook, O. (2009). Crater ice deposits near the south pole of Mars, Master's thesis, Massachusetts Institute of Technology. http://hdl.handle.net/1721.1/53113

White, O. L., Moore, J. M., McKinnon, W. B., Spencer, J. R., Howard, A. D., Schenk, P. M., et al. (2017). Geological mapping of Sputnik Planitia on Pluto. *Icarus*, *287*, 261–286. https://doi.org/10.1016/j.icarus.2017.01.011

Wieczorek, M. A. (2008). Constraints on the composition of the Martian south polar cap from gravity and topography. *Icarus*, *196*(2), 506–517. https://doi.org/10.1016/j.icarus.2007.10.026

Winebrenner, D. P., Koutnik, M. R., Waddington, E. D., Pathare, A. V., Murray, B. C., Byrne, S., & Bamber, J. (2008). Evidence for ice flow prior to trough formation in the Martian north polar layered deposits. *Icarus*, *195*, 90–105. https://doi.org/10.1016/j.icarus.2007.11.030

Yamashita, Y., Kato, M., & Arakawa, M. (2010). Experimental study on the rheological properties of polycrystalline solid nitrogen and methane: Implications for tectonic processes on Triton. *Icarus*, *207*(2), 972–977. https://doi.org/10.1016/j.icarus.2009.11.032

Zuber, M. T., Phillips, R. J., Andrews-Hanna, J. C., Asmar, S. W., Konopliv, A. S., Lemoine, F. G., et al. (2007). Density of Mars' south polar layered deposits. *Science*, *317*(5845), 1718–1719. https://doi.org/10.1126/science.1146995